Non-peer reviewed **Research Article** submitted to SEISMICA

Understanding fiber-optic sensitivity to a wavefield: A framework to separate site amplification from orientation effects

Olivier Fontaine * [1], **Andreas Fichtner** [2], **Thomas Hudson** [2], **Thomas Lecocq** [3], **Corentin Caudron** [1]

[1]Laboratoire G-Time, Departement of Geosciences, Environment and Society, Université libre de Bruxelles, 1050 Bruxelles, Belgium, [2]Department of Earth and Planetary Sciences, ETH Zurich, Zurich, Switzerland, [3]Seismology and Gravimetry, Royal Observatory of Belgium, 1180 Uccle, Belgium

Author contributions: *Conceptualization*: O. Fontaine. *Formal Analysis*: O. Fontaine, A. Fichtner, T. Hudson. *Writing - Original draft*: O. Fontaine. *Supervision*: C. Caudron, T. Lecocq.

Abstract When analyzing signals from Distributed Acoustic Sensing (DAS), the recorded amplitude across the array can be difficult to interpret, as it is influenced by many parameters. In this work, we explore the theoretical foundations of fiber sensing amplitude transfer functions. We begin with linear fiber segments and progressively extend to more complex geometries to create polarization filters. To build a filter from the gauge length we explore horizontal or vertical loops to average the signal over all azimuths or dips respectively. These geometries could cancel the component of the shear waves polarization contained within the loop plain. From these transfer functions, we explore the wavefield as seen by the DAS through a forward model based on ray theory. This model predicts the distribution of amplitude across a DAS array from a point source at low computational cost. The difference between our model and the measured wavefield relates to local site amplification, from which we derive an amplitude correction factor. The results, along with the foundational components of our approach, can be adapted for a broad range of applications, enabling novel sensing strategies. These include optimization of fiber deployment geometry, the creation of synthetic data, and the acceleration and refinement of existing location methods through amplitude and phase correction that account for the distinct sensitivity of DAS.

1 Introduction

The rapid advancement of Distributed Acoustic Sensing (DAS) is transforming the field of seismology. This technology enables the conversion of optical fibers into arrays of thousands of seismic sensors, pushing the frontiers in Earth sciences, e.g., in the monitoring of volcanic and glacial processes (Fichtner et al., 2026; Jousset et al., 2024; Nakano et al., 2024; Nishimura et al., 2021; Hudson et al., 2020; Walter et al., 2020; Fichtner et al., 2023), and the early

*Corresponding author: olivier.fontaine@ulb.be

detection of earthquakes and tsunamis (Yin et al., 2023; Lior et al., 2021). However, the nature of the wavefield sensed by DAS differs from the displacement sensed by seismometers (Kennett, 2024; Capdeville and Sladen, 2024).

To convert fiber into seismic sensors, the DAS interrogators inject coherent laser pulses at one end of the fiber. Along its path, small defects in the crystalline lattice scatter the laser pulse and a portion of this scattered wavefield travels back to the interrogator. The interrogator measures a phase shift in that backscattered light due to a relative change of the position of the scatterers in the fiber (Hartog et al., 2014). These changes are located using the two-way travel time of the laser pulse. Therefore, compared to displacement, DAS measures a spatial derivative, in the fiber direction (Daley et al., 2014), whereas seismometers record a time derivative of displacement. The relations between these measurement units and their respective sensing methods are portrayed in figure 1. This discrepancy in derivation is at the core of the unique sensitivity of axial strain sensing as observed already by Benioff (1935) and later in numerous DAS publications e.g., (Kennett, 2024; Martin et al., 2021; Vera Rodriguez and Wuestefeld, 2020; Wang et al., 2018; Bakku, 2015; Daley et al., 2014).

The strain recorded by DAS may vary as a function of several parameters. First, the interrogator averages the phase over a segment of the fiber, called a gauge length. This imposes a filter in the wavenumber domain, with a sinus cardinal (sinc) transfer function (Vantassel et al., 2022), effectively attenuating components of the wavefield whose wavelengths correspond to even fractions of the gauge length (Walter et al., 2020; Lindsey et al., 2020; Martin et al., 2018). Other parameters such as the fiber casing (Jiang et al., 2023), tension in the fiber (Xie et al., 2022), its coupling with the surrounding medium (Hudson et al., 2025a; Walter et al., 2020; Ajo-Franklin et al., 2019; Daley et al., 2014), as well as the physical properties of the medium itself (Celli et al., 2024; Ma et al., 2024), may also play non-negligible roles. Furthermore, recent studies suggest that the fiber has a strong response to heterogeneities in the earth's subsurface much smaller than the minimum considered wavelength (Capdeville and Sladen, 2024; Paitz et al., 2020).

The interplay of these parameters and the vast range of deployment possibilities highlight the importance of accurately understanding the DAS transfer function. This is particularly relevant for methods that depend on amplitude measurements, such as full-waveform inversion (Hudson et al., 2020; Luo et al., 2021; Noe et al., 2026), or amplitude-based event location (Nishimura et al., 2021). Moreover, understanding this transfer function can be leveraged to reduce the volume of data by focusing only on source-specific sensitive segments of the cable or guide future deployments through optimized fiber geometries (Fichtner and Hofstede, 2023).

Up to now, studies quantifying DAS amplitude and local amplification effects can be split into two categories. The first uses the Array Derived Dynamic Strain (ADDS), while the second is based on the Discrete Particle Scheme (DPS). Using a co-located seismometer array, ADDS reconstructs the strain-rate wavefield through finite-difference approximations of point velocity measurements (Muir and Zhan, 2022; Ichinose et al., 2022; Currenti et al., 2021; Wang et al., 2018). This approach was adopted in the early stages of DAS to assess the quality of the recorded waveforms using seismometers, as in Daley et al. (2016). In volcanic terrains, discrepancies between ADDS and DAS measurements were attributed to the presence of faults (Currenti et al., 2021). In the second method, DPS, the medium and the fiber are modeled by a network of interconnected particles. By changing the quality of the elastic bonds linking these particles, the local fiber response to a wavefield can be obtained (Hudson et al., 2025a; Celli et al., 2024; Jiang et al., 2023).

However, these two methods may not be adequate to keep up with the rapidly increasing diversity of fiber deployments. For instance, limitations arise when no seismic array with adequate geometry is available, or when elastic properties of the medium cannot be determined at a scale comparable to the high spatial resolution of DAS with an approachable computational cost. To build on the idea proposed in Kennett (2022), we address this gap in comparative measurements by examining the wavefield as it is "seen" by DAS, and compare a theoretical amplitude distribution along the fiber with actual recordings for a given source. The mismatch between the two provides an estimate of site effects.

2 Data and method

2.1 DAS sensitivity

To understand how different waves coming from different directions are recorded by DAS, we examine the axial strain-rate expression for different wave polarizations and fiber orientations. The full demonstration of those equations can be found in the supplementary materials.

To formulate our expression, we begin by defining a set of displacement polarization vectors for P, SV, and SH waves. Here, we consider a plane wave (ψ), as defined in equation 1, with amplitude A, propagating in the direction of the wavevector ($\vec{K}$) given by :

$$\begin{aligned}\vec{K} &= [k_x, k_y, k_z] \\ &= [\cos(\varphi_{ray})\cos(\theta_{ray}), \sin(\varphi_{ray})\cos(\theta_{ray}), \sin(\theta_{ray})]\end{aligned}$$

$$\psi(x,y,z,t) = Ae^{ik(ct - x\cos(\varphi_{ray})\cos(\theta_{ray}) - y\sin(\varphi_{ray})\cos(\theta_{ray}) - z\sin(\theta_{ray}))} \tag{1}$$

In equation 1, φ_{ray} and θ_{ray} describe the azimuth and the dip of the ray respectively, using polar coordinates, both defined to increase in the trigonometric direction. For a fiber segment oriented in the x direction, these expressions are derived in time then in space along the x axis to get the axial strain in the fiber axis. In this last step, we integrate two rotations to the strain tensor to align the xx component with any azimuth (φ_{DAS}) and dip (θ_{DAS}) of the fiber segment, becoming the xx' direction. The DAS azimuth and dip are also defined to progress in trigonometric direction. This gives us equations 2, 3 and 4 for point strain rate.

$$\dot{\epsilon}_{xx'P} = k^2 c\big(\cos\theta_{DAS}\cos\theta_{ray}\cos(\varphi_{DAS} - \varphi_{ray}) + \sin\theta_{DAS}\sin\theta_{ray}\big)^2 \psi(x,y,z,t) \tag{2}$$

$$\begin{aligned}\dot{\epsilon}_{xx'SV} =& k^2 c\big(-\cos\theta_{DAS}\sin\theta_{ray}\cos(\varphi_{DAS} - \varphi_{ray}) + \sin\theta_{DAS}\cos\theta_{ray}\big) \\ &\times \big(\cos\theta_{DAS}\cos\theta_{ray}\cos(\varphi_{DAS} - \varphi_{ray}) + \sin\theta_{DAS}\sin\theta_{ray}\big)\psi(x,y,z,t)\end{aligned} \tag{3}$$

$$\begin{aligned}\dot{\epsilon}_{xx'SH} =& k^2 c\cos\theta_{DAS}\sin(\varphi_{ray} - \varphi_{DAS}) \\ &\times \big(\cos\theta_{DAS}\cos\theta_{ray}\cos(\varphi_{DAS} - \varphi_{ray}) + \sin\theta_{DAS}\sin\theta_{ray}\big)\psi(x,y,z,t)\end{aligned} \tag{4}$$

Then, to consider the gauge length effect, we average these equations, over a linear segment in the fiber orientation

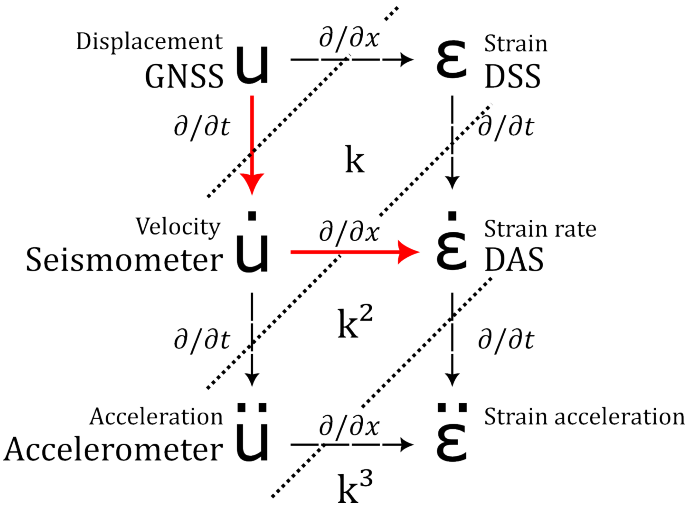

Figure 1 Relation between displacement (u) and strain (ϵ) with their relative time derivative and their means of measurement. Oblique delimitations isolate units with a similar number of derivatives and thus similar number of multiplications by the wavenumber (k) on their spectrum. For strain measurement, DSS stands for Distributed Strain Sensing.

rendering equations 5, 6 and 7.

$$\dot{\epsilon}_{xx'Pg} = \frac{2ck}{g}\left(\cos\theta_{DAS}\cos\theta_{ray}\cos(\varphi_{DAS}-\varphi_{ray}) + \sin\theta_{DAS}\sin\theta_{ray}\right) \times \sin\left[\frac{kg}{2}\left(\cos\theta_{DAS}\cos\theta_{ray}\cos(\varphi_{DAS}-\varphi_{ray}) + \sin\theta_{DAS}\sin\theta_{ray}\right)\right]\psi(x,y,z,t) \quad (5)$$

$$\dot{\epsilon}_{xx'SVg} = \frac{2ck}{g}\left(-\cos\theta_{DAS}\sin\theta_{ray}\cos(\varphi_{DAS}-\varphi_{ray}) + \sin\theta_{DAS}\cos\theta_{ray}\right) \times \sin\left[\frac{kg}{2}\left(\cos\theta_{DAS}\cos\theta_{ray}\cos(\varphi_{DAS}-\varphi_{ray}) + \sin\theta_{DAS}\sin\theta_{ray}\right)\right]\psi(x,y,z,t) \quad (6)$$

$$\dot{\epsilon}_{xx'SHg} = \frac{2ck}{g}\cos\theta_{DAS}\sin(\varphi_{ray}-\varphi_{DAS}) \times \sin\left[\frac{kg}{2}\left(\cos\theta_{DAS}\cos\theta_{ray}\cos(\varphi_{DAS}-\varphi_{ray}) + \sin\theta_{DAS}\sin\theta_{ray}\right)\right]\psi(x,y,z,t) \quad (7)$$

As suggested in Hudson et al. (2025b), a generalized S wave sensitivity can be obtained by combining the two polarizations using $\sqrt{\dot{\epsilon}^2_{xx'SHg} + \dot{\epsilon}^2_{xx'SVg}}$. Following Martin et al. (2018), for a wavelength much larger than the gauge length, its effect can be neglected and DAS strain rate is close to pointwise strain rate.

The axial strain-rate amplitude is controlled by quantities such as the wavenumber, gauge length, and velocity. In addition, and central to this paper, it is affected by a geometric effect arising from the relative orientation between the fiber and the wavefield. In the following part, we call this angular dependency the 'fiber sensitivity'. To illustrate these terms we suggest three kinds of visualization visible in figure 2 for a fiber along the y-axis (azimuth = 0°) with a dip of 45°. In the left column, we consider this sensitivity from a source perspective. In a homogeneous 1 km^3 cube , with the fiber in its center, we distribute sources evenly throughout the surrounding space. Each pixel in this space contains a source and is colored following the amplitude it can generate in the fiber for a specific polarization, using a straight ray. When plotting our cubes, only the outer surfaces are colored to enhance visibility. In the central column, the same geometrical factor is visualized as a volume surrounding the fiber. Lastly, in the right column we suggest a polar projection, with the center containing rays coming from the bottom. The outer rim contains the rays coming from the top. We also normalized the amplitude to 1 to the maximum value on each display.

For both P and S waves, the sensitivity preserves its 2D relation of $\cos^2(\varphi_{\text{ray}})$ and $\sin(2\varphi_{\text{ray}})$, but forming a solid of revolution around the fiber axis. This relation is clearly visible in the volumetric view, in the central column of figure 2. However, the relative contributions of the SV and SH components vary significantly with the dip. As the sensitivity to SH waves decays proportionally to $\cos(\theta_{\text{DAS}})$, it will reach zero for a vertical fiber. Consequently, SV waves exhibit a strong azimuthal constraint for a horizontal fiber. This azimuthal constraint gradually disappears as the fiber dip increases, resulting in sensitivity to all azimuths for a vertical fiber. The equations 3, 4, 6 and 7 also predict the spatial distribution of polarity inversion for the different shear-wave polarizations. This complex sensitivity to shear waves can yield strong information on the source orientation as in Luo et al. (2021) but require acute knowledge of the fiber geometry.

2.2 Integration of DAS sensitivity in a ray based framework

In this section, we expand beyond a plane wave sensitivity model from last chapter, to consider arbitrary source mechanism. For this, we integrate our sensitivity analysis to a wavefield framework based on ray theory, accounting for various source descriptions.

To model the propagation of waves, we use Pykonal (https://malcolmw.github.io/pykonal-docs/). This open-source Python package is designed to calculate travel-time grids by numerically solving the Eikonal equation using the Fast Marching Method (FMM) (White et al., 2020). This method enables efficient computation of first-arrival travel times in both 2D and 3D domains, supporting spherical and Cartesian coordinate systems. To propagate rays through the travel time grid, Pykonal uses the path of steepest descent, from the source to the receiver using Euler's steps (White et al., 2020). Compared to traditional ray-based approaches, like the shooting or bending methods, a grid-based approach offers greater numerical stability and is well suited to handle complex 3D velocity models (Rawlinson et al., 2008). However, by design, it can only account for the first arrival.

To implement this framework to our test case, Brady Hot Springs (BHS), we used the 3D velocity model from Zeng et al. (2017), with an original resolution of 25 m. We applied a low-pass filter to the velocity model, with 99% attenuation at 10 wavelengths (Liu and Schmitt, 2006). The filter parameters are based on a 5 Hz signal (see Section 2.3) traveling at 0.6 km/s. This ensures that the high-frequency assumption required for ray theory is satisfied. Because the travel time grid resolution and ray tracing step-size, e.g. Euler's steps, are related to the velocity model resolution, we tested the grid sampling parameters to reduce the computational cost. The details of these tests can be found in the supplementary materials. We observed that, the ray is stable up to a step size of half of the smallest object preserved by the low-pass filter. In the same experiment, measuring the angles between the rays at the source and receiver across varying velocity grid spatial sampling, yields a variation of angular errors of 0.59° at the source and 3.30° at the receiver. We quantify the uncertainty on the forward model based on these values. We do so by creating a population of 100 realizations, introducing in each a random perturbation at the source and receiver terms distributing the error evenly between the azimuth and dip. We estimate the forward-model uncertainty as the standard deviation of these 100 realizations. In our case, the error is primarily influenced by distance spreading and accounts for 17.9% of the amplitude value on average.

Finally, to describe the source, we utilized the direction- and polarization-dependent amplitudes for a given moment tensor from Aki and Richards (2002). For our model, to keep the polarization simpler, we used a far field approxima-

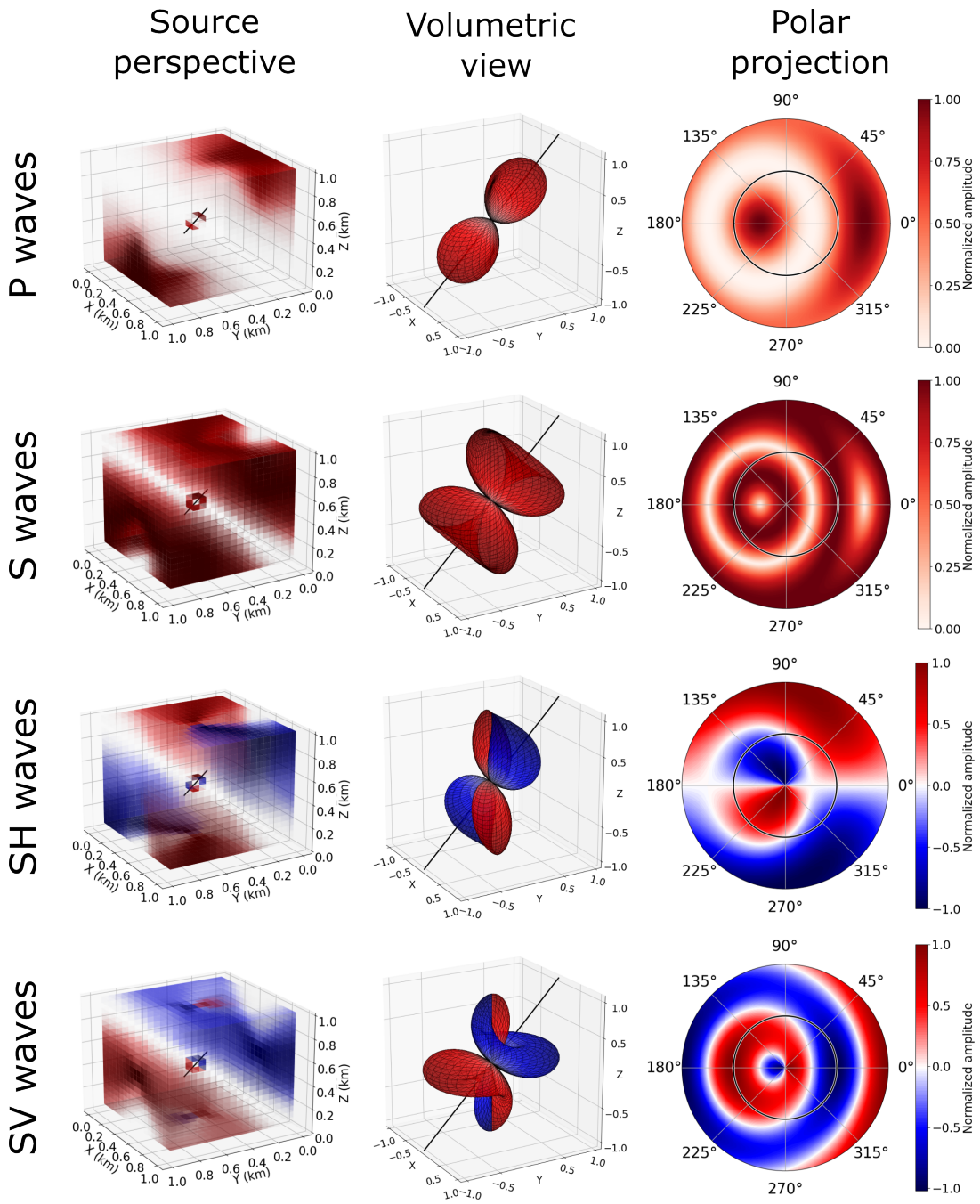

Figure 2 Representation of the broadside sensitivity of a fiber to body waves. The fiber, shown as a black line in the left and central columns, has a dip of $45°$ and an azimuth of $0°$. The representations are based on equations 2, 3, and 4 and consider a wavelength much larger than the gauge length. The S-wave amplitude is computed as $\sqrt{\dot{\epsilon}^2_{xx'SH} + \dot{\epsilon}^2_{xx'SV}}$. The left column illustrates the sensitivity for sources homogeneously distributed around the fiber in a homogeneous medium; each pixel is colored according to the amplitude recorded by the fiber in the center of the cube for a source located at the pixel for a given polarization. The central column presents a volumetric representation of the fiber broadside sensitivity to body waves, while the right column shows the corresponding polar projections. In these polar plots, rays arriving from below are mapped to the center, horizontal rays are indicated by the black circle, and vertically incident rays from above are located at the outer rim. All plots are normalized by their respective maximum values.

tion. Therefore to reduce the influence of the near field in the data, important for the region with source-receiver distance equal or smaller than a wavelength (Lokmer and Bean, 2010), we kept the data in its original unit, strain rate. Owing to the spatial derivative to move from velocity to strain rate, visible in figure 1, the resulting spectrum is closer to acceleration, decreasing low frequency, therefore long wavelength, amplitudes.

2.3 DAS Data measurement and processing

Having developed a model that allows to understand the amplitude variation recorded across a fiber array for a given source, we wish to validate it. To this end we, we chose the data from the Poroclastic Tomography experiment (PoroTomo) (Feigl, 2019) as it is open-source and features a fiber with complex geometry and controlled sources.
This multidisciplinary experiment took place in 2016 at BHS geothermal field (Nevada, USA). During the experiment, a DAS fiber was deployed horizontally (DASH) in a zigzagging trench approximately 1 m deep, visible in figure 3. Offering many angles, its geometry is ideal to test broadside sensitivity, while it also crosses various geological features, possibly generating varying site effects. The geology of BHS is composed of a Mesozoic crystalline basement rock (around 1400 m depth) capped by a succession of sedimentary and volcanic formations from the Miocene, together forming the bedrock (Siler and Pepin, 2021). It is covered by 50 m of sedimentary deposits (Miocene to Pleistocene) observed during the PoroTomo experiment by a sharp velocity contrast with the bedrock formation (Zeng et al., 2017). These formations are crossed by a network of normal faults, with a general SSW-NNE orientation. Faults have already been shown to impact strain amplitude measured by DAS in many occasions (Ma et al., 2024; Currenti et al., 2021; Jousset et al., 2018).

During the PoroTomo experiment, a variety of signals were recorded, from both active vibroseis sources and natural events (Wang et al., 2018). In this work, we decided to focus on the active seismic experiment, as it gathered 6633 catalogued events characterized in source location and mechanism. The vibroseis signals generated by the vibrotruck consist of 20 s sweeps ranging from 5 to 80 Hz. For our sources, we selected 9 sites across the array, visible in figure 3, each counting 9 sweeps. The sweeps can be of 3 types; compressional (P), shear transverse (ST) and shear longitudinal (SL), every site counting 3 of each sort.
These signals were recorded using a Silixa iDAS with a gauge length of 10 m and a spatial sampling of 1 m at 1 kHz. Preprocessing includes removing common-mode noise (Lindsey et al., 2020) and applying a bandpass filter between 3 Hz and 20 Hz. To enhance the signal-to-noise ratio (SNR) and reduce the volume of data, channels are grouped and linearly stacked in sets of 11. Then we downsample after band passing, using a mean, to 100 Hz. After preprocessing, we used a trigger on each sweep to capture the onset of the signal. For this, we employed the Modify Energy Ratio (MER) from Han et al. (2009). Because of the large energy difference between the channels, up to 22.69 dB across tens of channels, as can be seen in figure 4, identifying a fixed threshold for a trigger proved challenging and those had to be re-optimized for each event. Instead, we chose the percentiles 65 of the MER values for each DAS channel, to achieve a data-driven trigger level. To ensure the quality of the picking, each trigger must be within 0.5 s of its neighbors, 3 s of the mean timestamp of all triggers. The triggers not meeting these criteria are redefined as a linear interpolation of the two closest valid trigger. After obtaining the initial arrivals, the signal amplitude is measured using a 0.3 s RMS window. An example of these triggers and quality criteria are displayed in figure 4. To ensure that

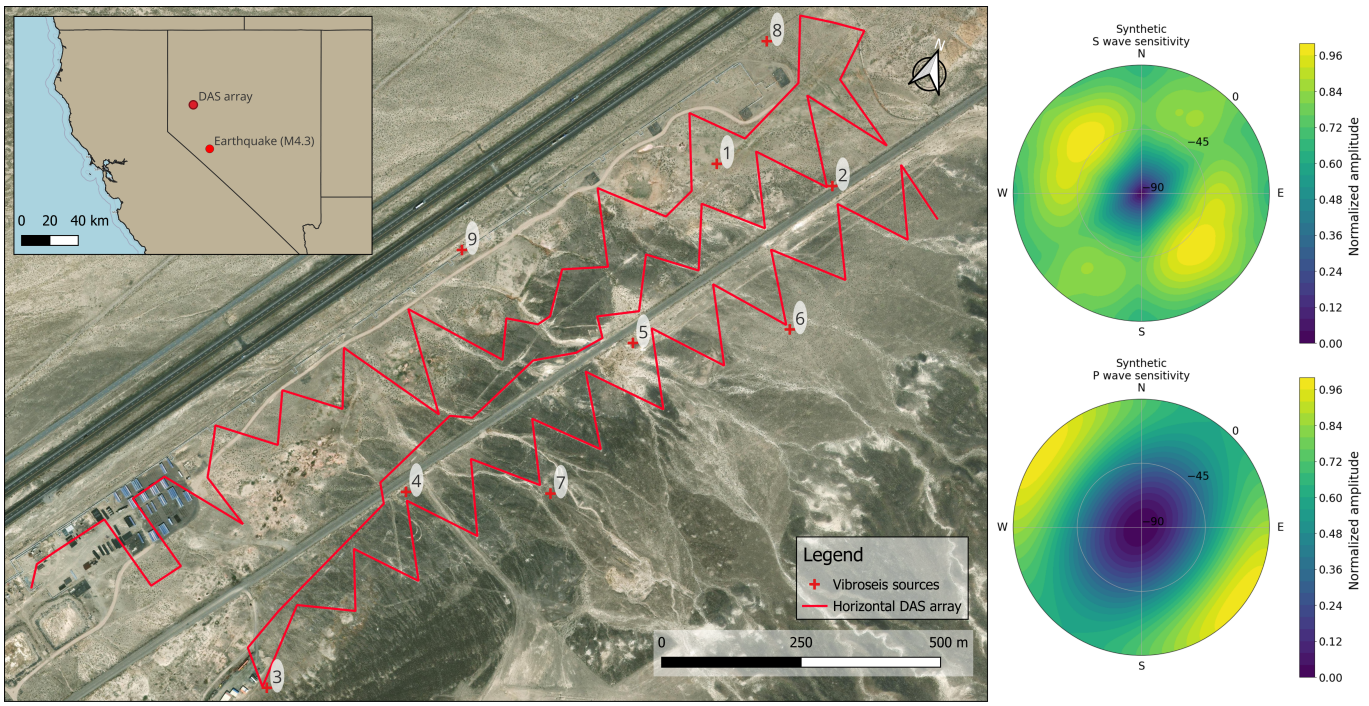

Figure 3 Map of the PoroTomo DAS fiber deployment (red line) and the Vibroseis sources used in this study (red crosses). The top-left inset shows the location of Brady Hot Springs in Nevada, as well as the location of the magnitude 4.3 earthquake used to compare our site-effect analysis. On the write, the synthetic spatial sensitivity for the PoroTomo horizontal DAS array, illustrating the directional response to seismic waves as a function of azimuth and incidence angle (dip). The top polar plot shows the corresponding average S-wave sensitivity across all individual channels in the array, while the bottom polar plot presents the average P-wave sensitivity. Both polar plots are normalized by their respective maximum values.

the amplitude measured is the one of the passing wavefield and not a local noise source, only channels with a SNR greater than 2 are included in the analysis.

3 Results

3.1 From a DAS channel to the space around it

3.1.1 DAS array summary

To assess the overall broadside sensitivity of a DAS array, we construct a synthetic sensitivity polar projection by averaging the individual responses of all channels. An example for the DASH from PoroTomo is presented in figure **??** for both P and S waves.

Based on the BHS fiber layout, P waves should be, on average, better recorded if traveling horizontally in the NW-SE axis, with an overall poor recording for steep rays. In comparison, S waves can be recorded at a much steeper angle, with a maximum at around 45° in the NW-SE direction. For both polarizations, a perfectly vertical ray should not be recorded if we only consider the direct axial strain. We also note that these projections do not inform us about the influence of any local velocity structure .

3.1.2 Impact of a layered medium on fiber sensitivity

Using our ray-based DAS sensitivity framework, we examine the effects of a layered velocity model on the recorded amplitude by the fiber. The test configuration consists of a 1 km^3 cube divided into two layers of equal thickness. The upper layer is 50% slower than the underlying layer. A fiber is embedded within the upper layer, it is oriented along the y axis. To look at the impact of its dip on the spacial amplitude response we consider 3 cases: horizontal, 45°, and

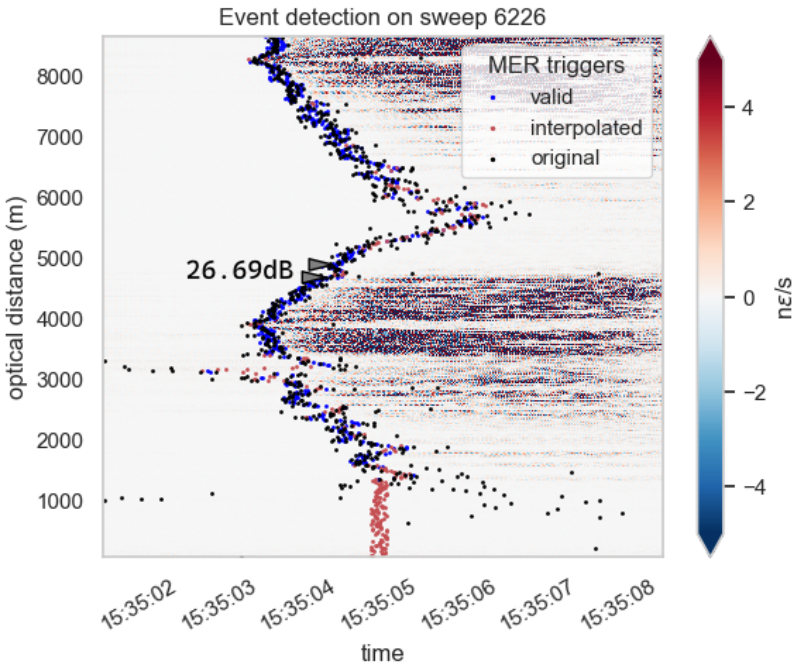

Figure 4 Example of a DAS record (Sweep 6226, Site 2) expressed in nanostrain-rate ($n\epsilon/s$) with triggers obtained using the Modified Energy Ratio (MER). The original triggers are shown as black dots. Blue dots indicate valid triggers, while red dots represent interpolated triggers. The amplitude difference of 26.69 dB is measured between 4634 m and 4997 m.

vertical. Sources are evenly distributed throughout the model space. For each source, we perform ray tracing and colored the pixel containing the source according to the recorded amplitude in the fiber for a given wave polarization. In these models, we only focus on the geometrical relation between the wavefield and the fiber and each result is normalized to 1. These results are displayed in figure 5.

For a P-wave, the dip of the fiber strongly influences the layer to which it is the most sensitive. If horizontal, the sensitivity is predominantly within the upper layer, in an area aligned with the fiber orientation. However, if vertical, the fiber can sense the entire bottom layer. The 45° dipping configuration, provides a transitional response, exhibiting sensitivity to both the upper and lower layer, but on the opposite side.

The spatial sensitivity of S waves results from the combined contributions of both SH and SV components and can be understood through those two. For SH waves, the azimuthal 45° sensitivity and polarity inversion are clearly visible. In the case of a horizontal fiber, this sensitivity is primarily confined to the upper layer. As the dip increases, sensitivity and the shadow zone inline and orthogonal to the fiber axis spreads through the lower space. This results in blindness in half of the lower space and inline with the fiber. Finally, as expected by equations 4 and 7, there is no vertical axial strain from an SH wave. In contrast, SV waves are primarily sensed along the fiber direction for a horizontal deployment , with the velocity contrast broadening the footprint of the lower lobes in the bottom layer. As the dip increases to 45°, the sensitivity expands laterally and the polarity inversion tends to happen at the boundary between the model layers. When the fiber is vertical, it exhibits sensitivity in all azimuths throughout most of the lower layer, except directly beneath the fiber along its axis. The upper layer, compared to the lower layer, is almost not sensed.

For vertical fiber for both P and S wave, sensitivity in the upper most parts of the top layer seems unexpectedly high and better inline with the Cartesian system. We could attribute this effect to an error in the ray tracer as those high

sensitivity zones stay in the same position even when rotating the fiber. Hence no source or receiver should be placed on the edges of the velocity model to ensure the quality of the ray tracing.

3.1.3 Looped Gauge Length

Seeing the spatial distribution of the polarity inversion for shear waves, and since DAS averages the wavefield over a gauge length, we wondered if this uniqueness could not be turned in an analog polarity filter. For this we explored the idea of a looped gauge length in the horizontal or vertical plane, to average the wavefield over all azimuths or dips, respectively. To build these new expressions we started from the equations 2, 3 and 4, for a linear fiber. For simplicity, we assume a large wavelength-to-gauge length ratio such that the DAS response approaches a point strain-rate measurement. For a vertical loop, we average over all dips by solving $\frac{1}{g}\oint \dot{\epsilon} d\theta_{DAS}$ for P, SV and SH waves yielding equations 8, 9 and 10 respectively.

$$\dot{\epsilon}_{Pvl} = \frac{k^2 c}{2r}(\cos^2(\theta_{ray})\cos^2(\varphi_{DAS} - \varphi_{ray}) + \sin^2_{\theta_{ray}})\psi(x,y,z,t) \tag{8}$$

$$\dot{\epsilon}_{SVvl} = \frac{k^2 cA}{4r}\sin(\theta_{ray})\sin^2(\varphi_{DAS} - \varphi_{ray})\psi(x,y,z,t) \tag{9}$$

$$\dot{\epsilon}_{SHvl} = \frac{k^2 c}{4r}\cos(\theta_{ray})\sin(2(\varphi_{DAS} - \varphi_{ray}))\psi(x,y,z,t) \tag{10}$$

For a horizontal loop we average over all azimuth using $\frac{1}{g}\oint \dot{\epsilon} d\varphi_{DAS}$, for P, SV and SH waves giving equations 11, 12 and 13

$$\dot{\epsilon}_{Phl} = \frac{k^2 c}{2r}\cos^2(\theta_{ray})\psi(x,y,z,t) \tag{11}$$

$$\dot{\epsilon}_{SVhl} = \frac{-k^2 c}{4r}\sin(2\theta_{ray})\psi(x,y,z,t) \tag{12}$$

$$\dot{\epsilon}_{SHhl} = 0 \tag{13}$$

The resulting expressions are visualized in figure 6, with detailed derivations provided in the supplementary materials.

Based on these new equations, in the case of a horizontal loop, the sensitivity to both P and SV waves loses its azimuthal constraint, while the dip dependency remains unchanged. In contrast, SH waves are effectively canceled due to the average with the polarity inversion. For a vertically oriented loop, P-waves retain their typical azimuthal sensitivity, but it becomes distributed across all dip angles. SH waves exhibit a similar response as in a horizontal linear fiber. SV waves, however, appear to be canceled in the loop direction, yet new sensitivity lobes emerge at a +/- 45° dip to the normal of the plane containing the loop.

3.2 From a point in space to the fiber array

3.2.1 Masurement of site effect

By using our forward model to predict the recorded amplitude of a given source through a DAS array and comparing it with the amplitude of the recorded wavefield, we approach a measurement of amplitude anomalies and local site effects. An example of recording and forward model and their difference is given in figure 7. To compare our

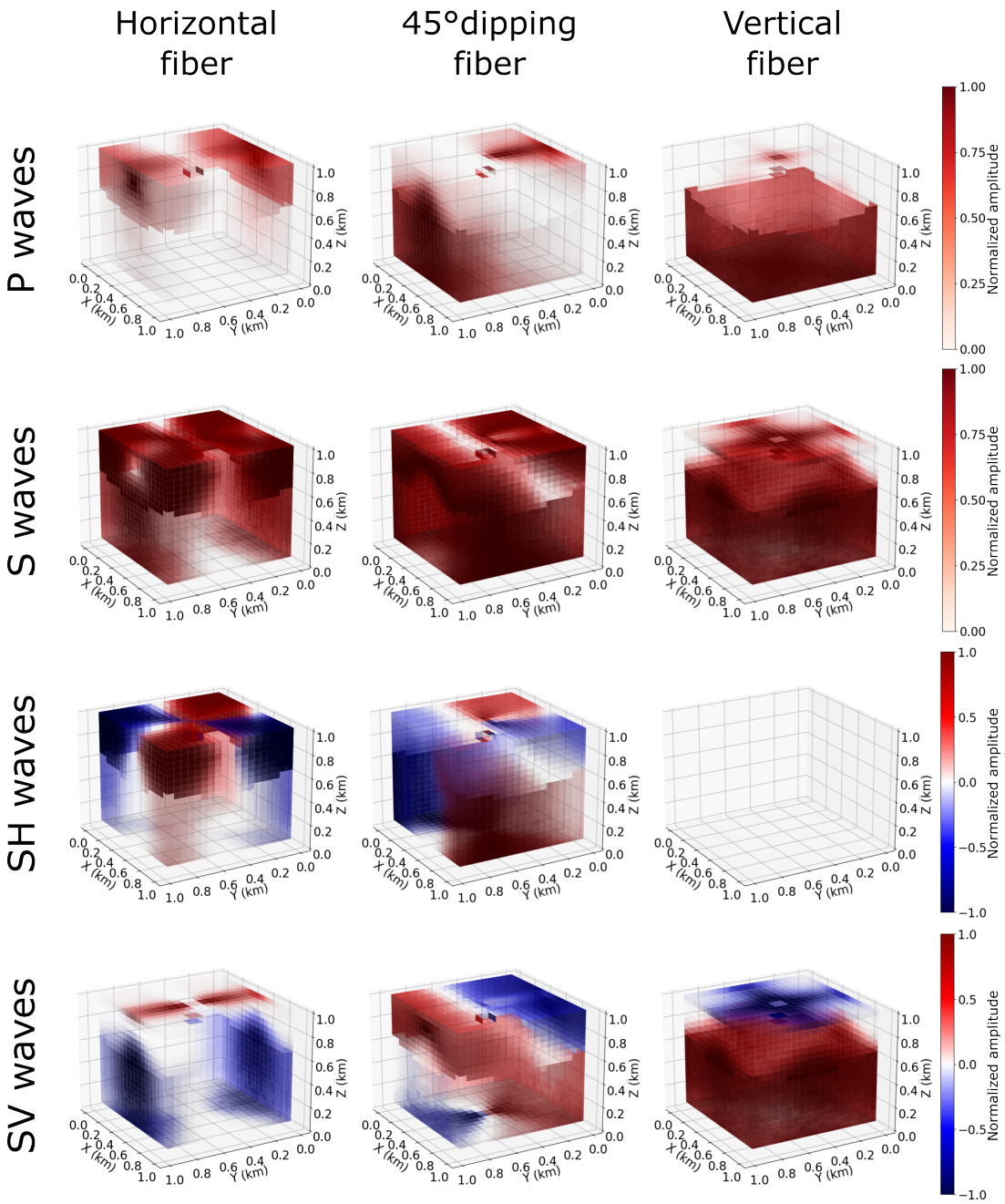

Figure 5 Impact of a layered medium on the amplitude sensitivity of a fiber to body waves. The model consists of a 1 km^3 volume divided into two layers of equal thickness, with the seismic velocity in the top layer set to 50% lower than in the lower layer. Each pixel is colored according to the ability of a source at that location, for a given body-wave polarization, to generate amplitude in the fiber. For each polarization, 3 DAS channel orientations are considered: horizontal (left), 45° dip (center), and vertical (right). Therefore, the central column is the equivalent of the left one in figure 2 with the introduction of a velocity contrast. In these plots, only the outer surfaces of the volume are displayed for clarity, and each plot is normalized by its maximum value.

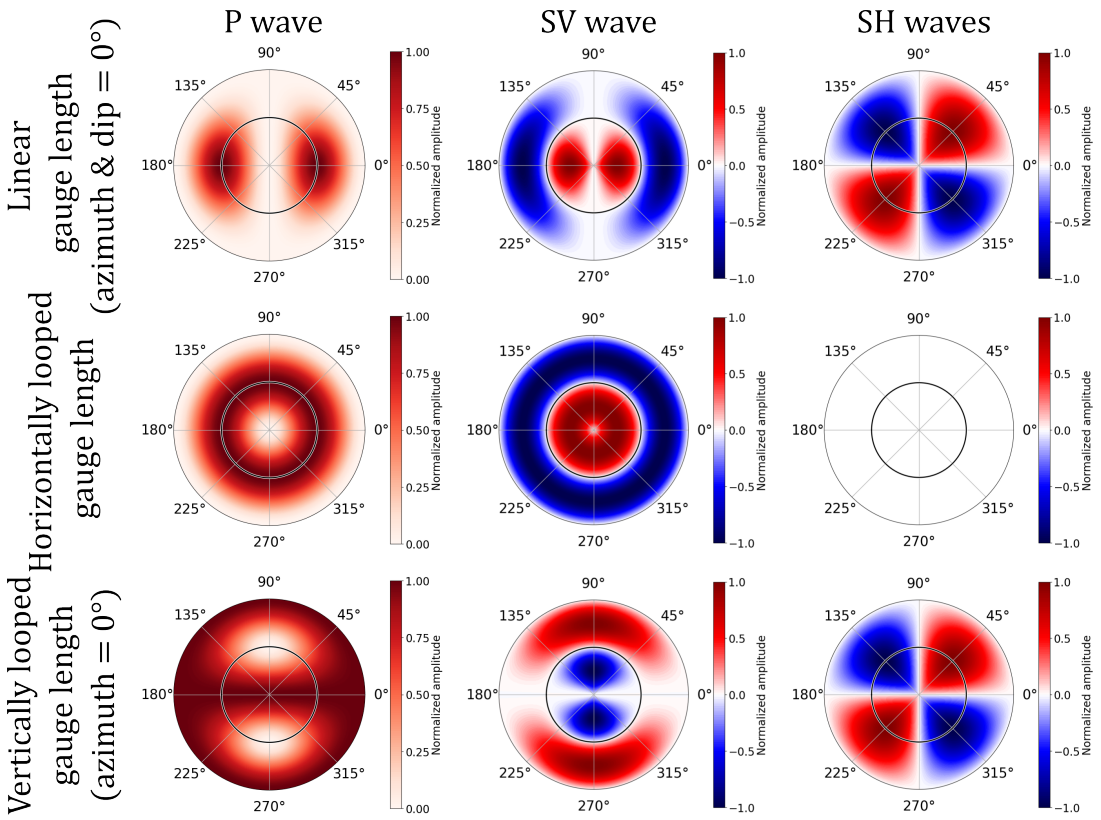

Figure 6 Orientation specific amplitude response of looped and linear gauge length to body waves. These figures are based on the equations in table **??**, and consider a wavelength much larger than the gauge length. In these polar plots, rays arriving from below are mapped to the center, horizontal rays are indicated by the black circle, and vertically incident rays from above are located at the outer rim. All plots are normalized by their respective maximum values.

model to the measurement, we use a weighted linear regression in a log-log space, as displayed in figure 8, where the weights correspond to the forward model estimated errors. Using double-logarithmic axes, homogenizes the distribution of points for our linear regression. We further homogenized this distribution by median-binning along the measured amplitude axis, yielding 200 evenly spaced points in logarithmic space. For each bin, the corresponding error is defined as the median of the individual point errors within the bin. Secondly, residuals in log-log space are relative by nature. This implies that they can be interpreted as a scaling factor by raising them to the power of the base of the logarithm. In other words, a log residual of 1 in $log_{10} - log_{10}$ space is a scaling factor of 10^1 due to site effect amplification. For each linear regression, we also extract the standard deviation of all the residuals as a measure of error on the amplitude scaling factors.

Overall, the median R^2 of the linear regressions on the binned data over the 81 sweeps is 0.67 and is evenly distributed between source types; P (compressional), ST (shear transverse) and SL (shear longitudinal). However, the R^2 is unevenly distributed between locations. For instance, the sites 8 and 9 are poorly constrained by the models. For the other sources, R^2 tends to improve as they are further from site 7. The values for the different source types and locations are summarized in table 1.

To reduce the error on the amplitude scaling factors, we combine 68 of the 81 sweeps with $R^2 > 0.4$, by taking their median. We estimate the error of the median by bootstrapping our scaling factor population and added to each a random perturbation defined by their respective error, before taking their median. The error is estimated as the standard deviation of these realizations. The residual pattern reveals distinct outlying regions but also zones without

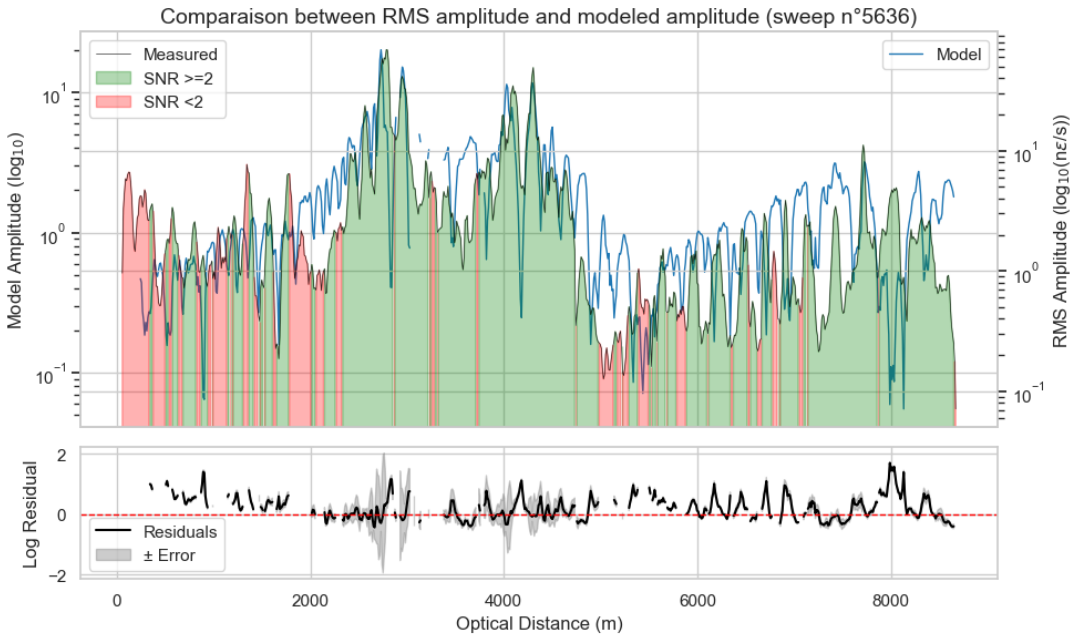

Figure 7 Comparison between modeled and measured amplitude distributions across the DAS array for sweep 5636, and the amplitude correction associated with local site amplification. In the top panel, the modeled (forward) amplitudes are shown in blue and the measured amplitudes in black. Measurements are separated into regions with SNR > 2 in green and < 2 in red. The bottom panel shows the residuals from a linear regression, as in figure 8. Only data with SNR > 2 are used to compute these residuals. These logarithmic residuals correspond to scaling factors associated with site-effect amplification. The gray shaded area around the log residual represents the uncertainty arising from ray-tracing errors of that scaling factor.

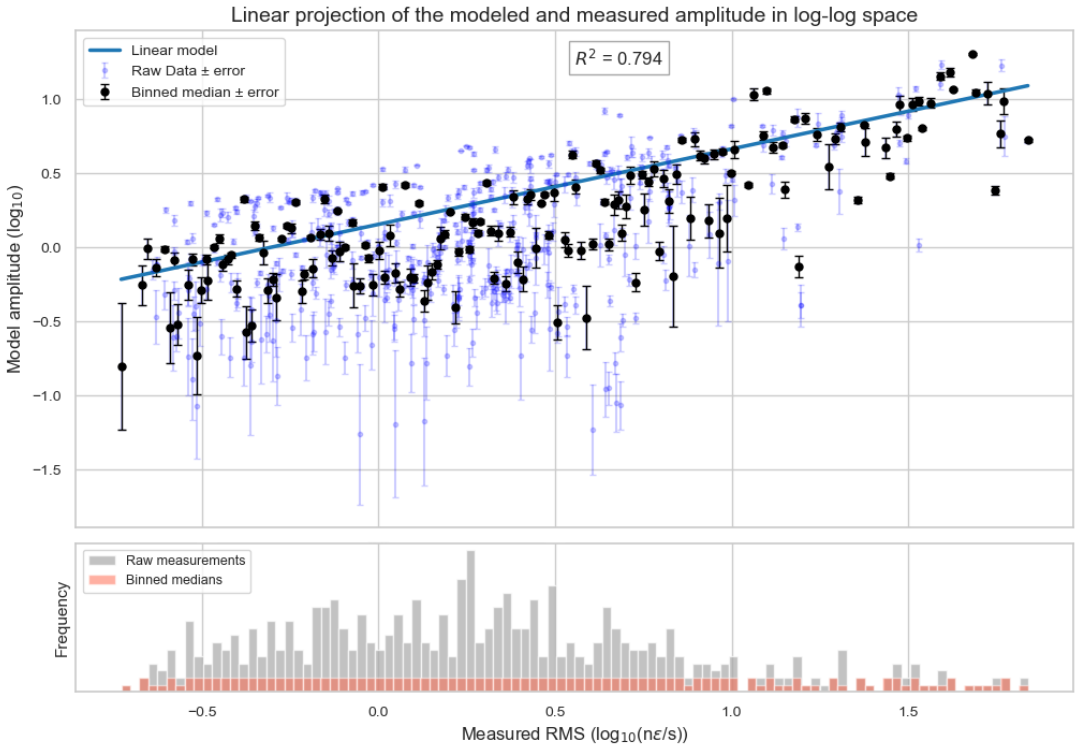

Figure 8 Extraction of amplitude scaling factors from modeled and measured amplitudes using linear regression for sweep 5636. The top panel shows a weighted linear regression in logarithmic space between measured and modeled amplitudes. The residuals relative to this regression define the amplitude scaling factors. The regression weights are given by the uncertainties from the forward model. To homogenize the measured amplitude distribution, the original data (blue) are median-binned, yielding the black points used in the regression. The bottom panel shows the density of amplitude measurements, with the original distribution in gray and the binned distribution in red.

residuals, both visible in figure 9. Logarithmic residuals range from –0.33 to 0.88, with a median error of 0.15. The majority of fiber residuals are on the order of their relative error and only the strong outliers rise above the noise level. If we compare the location of these outliers to the amplitude response of the M 4.3 earthquake, whose amplitudes distribution is dominated by site effect following Wang et al. (2018), we find a strong resemblance. This similarity is displayed in figure 9. Concerning the zone without any residuals, it extends on the north side of a fault crossing all the array from Northwest to Southeast, visible as a black dash line in figure 9. This arises from a lack of clear arrival with a SNR above 2 indicating strong modification of the wavefield around this geological boundary.

Table 1 Sources and sites model statistics. Sources can be compressional (P), shear transverse (ST) and shear longitudinal (SL). The sites are visible in figure 3

Statistic	Source P	Source SL	Source ST	Site 1	Site 2	Site 3	Site 4	Site 5	Site 6	Site 7	Site 8	Site 9
Median	0.673	0.676	0.643	0.761	0.801	0.698	0.617	0.713	0.731	0.491	0.439	0.312
Std	0.207	0.244	0.147	0.050	0.069	0.128	0.109	0.200	0.121	0.239	0.175	0.140
Min	0.168	0.011	0.212	0.676	0.677	0.489	0.421	0.212	0.438	0.011	0.261	0.168
Max	0.891	0.849	0.833	0.833	0.891	0.891	0.746	0.780	0.822	0.643	0.756	0.598

4 Discussion

4.1 The impact of fiber orientation on its sensing capacities

By creating a framework to investigate a wavefield as "seen" by DAS, we could understand the amplitude variation observed across the array. Where the prediction failed, the method highlighted site effects. The spatial distribution of these site effects coincides with the amplitude anomalies observed for an M 4.3 earthquake. Yet, we still observe discrepancies between the forward-modeled and measured amplitude patterns not attached to site effects. These differences may arise from the limitations of the ray tracing, which does not account for later arrivals. At BHS these later arrivals could include reflections in between fault planes, which might be better sensed in the fiber than the direct wavefield. We also note a significant loss of amplitude after crossing some faults, not included in the model. Surface effects and surface waves are similarly not considered. On the source side, the signal from the vibroseis was not always detectable across the full array, reducing the amount of usable regression points and lowering the R^2 for some of the linear regressions. Stronger sources, such as regional earthquakes, could improve the model if available in the dataset. Alternatively, ambient noise could be used, although this would be based on surface waves. Overall, the complexity of the wavefield in the geology of BHS leads to large variations between the predicted and observed signals, contributing to the generally large uncertainties on the the scaling factor. The evolution of the R^2 values illustrates this behavior, increasing from 0.49 to 0.80 as the distance from the site 7, the most affected region by site effects, increases. Developing a full-waveform model could help quantify the importance of all the elements not considered in our model in the case of a boundary-rich environment such as BHS.

When measuring the amplitude difference with our model, we introduced a bias in our data. The amplitude picking method relies on detecting an amplitude increase between forward and backward windows, and we only retain channels with SNR above 2. However, if we had channels decoupled from the wavefield, for instance located in a conduit, they would not have been picked and considered here. By quantifying the energy of the source, we could characterize the sensitivity losses and not only the gains. Also, when a correction factor is produced, we note that

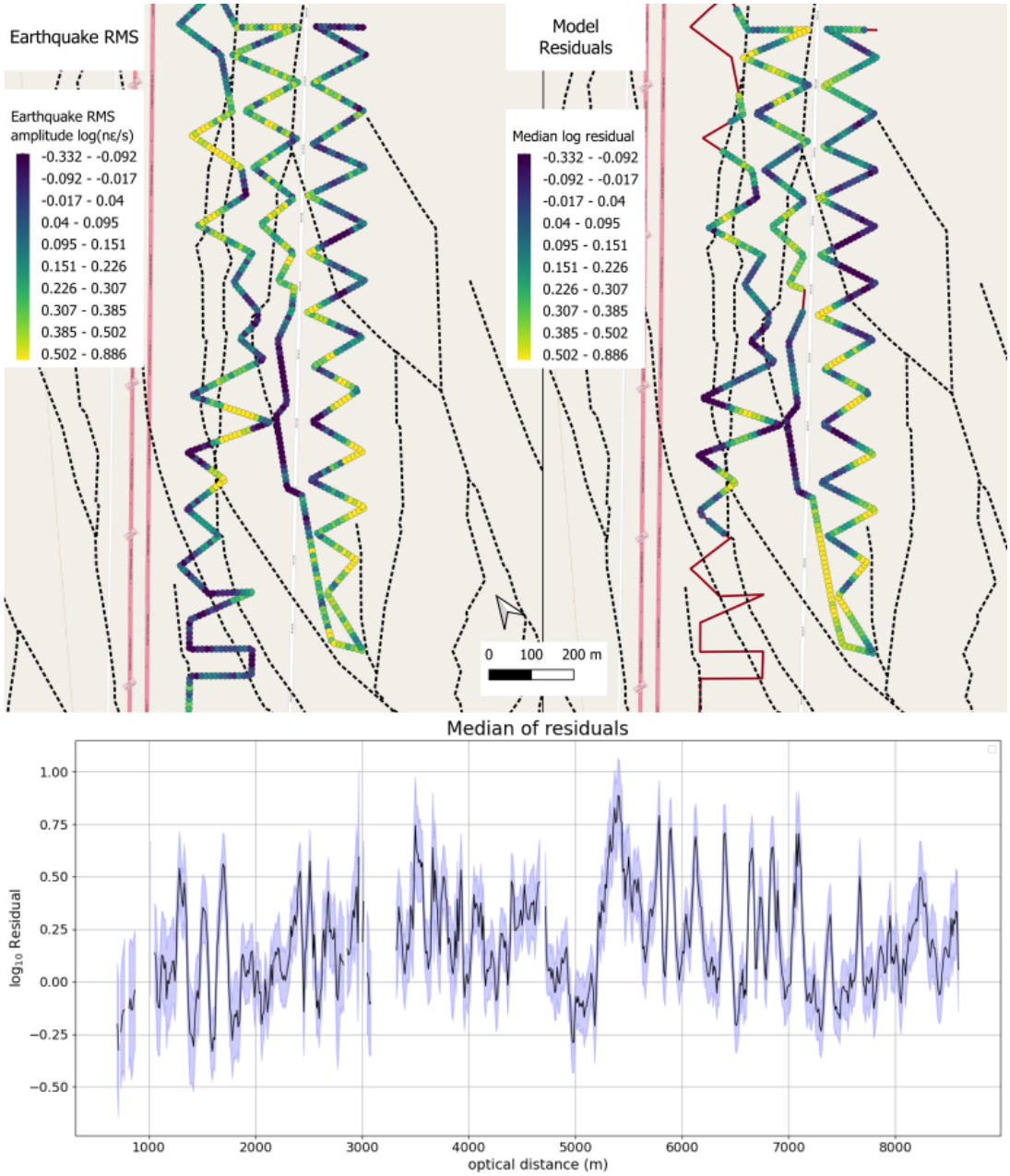

Figure 9 Comparison between the estimated site amplification factors and the measured amplitudes of the M 4.3 earthquake. In the top panel, the left plot shows the earthquake amplitude expressed as $log(n\epsilon/s)$, while the right plot shows the median of the log-residuals (i.e. the scaling factors for site amplification) computed across the 9 sites. Areas with no displayed data correspond to locations where fewer than 30 sweeps had SNR > 2. The bottom panel shows the same log-residuals as a function of optical distance, along with their relative uncertainties.

the residuals are tied to the average sensitivity of the array. This makes them unsuitable for inter-array comparisons or as an absolute amplitude correction factor.

4.2 Future perspective

For this experiment, we used a DAS sensitivity model to detect amplitude outliers and generate an amplitude correction factor. However, the travel-time grid and amplitude patterns we produce could support additional applications. For instance, when training deep neural networks for earthquake detection and phase picking, synthetic datasets could be built by convolving event waveforms with relative time and amplitude information from the model. This would allow for unbiased training regardless of the availability of earthquakes, while remaining at fairly low computational cost. At BHS, we tested the sensitivity of an existing array, but we could also evaluate hypothetical arrays and integrate these results for future deployment planning (Fichtner and Hofstede, 2023). Furthermore, for any array, the DAS shadow zones could be mapped to guide the placement of seismometers and fill the blind spots. A deeper understanding of DAS transfer function also highlights that blind spots themselves can carry valuable information. These could be incorporated in an amplitude look-up table for pre-grid search optimization, reducing computational effort. One last application of our model is in f-k analysis to solve a problem encountered in Lindsey et al. (2017). By assigning the model's amplitude sign to the corresponding elements of the steering vector, the polarity inversion of shear waves would be accounted for, making the stacking operation constructive again. Finally, our work on the polarization filter of looped gauge lengths remains theoretical. Field deployments will be needed to validate the concept. If these proved to be efficient, these features could be integrated in new arrays for shear wave polarization analysis. Another application could be in filtering surface waves using horizontal loops. Seeing the broadside sensitivity to P and SV waves but the absence of SH waves, the gauge length effect could be used as an analog filter for Love waves and omnidirectional sensors for Rayleigh waves. If proven efficient, these looped gauge length could build a bridge between rotational seismology and DAS.

5 Conclusions

In this work, we consider the impact of the fiber orientation on its capacity to record the amplitude of body waves coming from different directions. Compared to previous studies, we derived a single equation describing the transfer function of a linear gauge length with any dip and azimuth. Through it, we gained an understanding of the amplitude recorded by a DAS at the scale of an array but also to looped gauge length that could be used as shear waves polarization filters. When combining this knowledge with ray tracing tools, we could investigate the capacities across the array to recover the amplitude of a source. From the amplitude difference between the forward modeled and the recording, we could separate the effect of fiber orientation and site effects at low computational cost. This quantification of the site effect gave us an array specific amplitude correction factor. However, due to the complexity of the wavefield in BHS, not captured by our model, our amplitude rescaling retain large error. This forward-modeling perspective also allows us to examine from a fiber segment, its ability to capture sources in its surrounding space. In particular, it emphasizes the interplay between the velocity structure and gauge length orientation. In summary, by exploiting the known directional sensitivity of DAS, we draw new insights from amplitude variations along the fiber array, treating energy loss as equally informative as energy gain in interpreting the wavefield.

Finally, from our model's time and amplitude information, we could support many new applications encompassing grid search optimizations, creation of waveform synthetic at low computational cost and beamforming.

Acknowledgements

We thank Daniel Bowden and the Observational Seismology group at ETH Zürich for the initial discussions that inspired this project. We are also grateful to Pascale Edme for valuable insights on the free-surface effect, and to Társilo Girona for his helpful feedback on the manuscript.

This research was supported by the Fonds de la Recherche Scientifique (FNRS, contract number FC 49429). We further acknowledge the use of `DASPy` (Hu and Li, 2024) and `PyKonal` (White et al., 2020). We also thank the developers of Python, NumPy and Matplotlib.

Data and code availability

All codes developed and used in this study—specifically those applied to the Brady Hot Springs dataset, including the implementation of a rotated Cartesian reference system—are available at : https://zenodo.org/records/18863370?preview=1&token=eyJhbGciOiJIUzUxMiJ9.eyJpZCI6IjlhOGI0ODczLTIxYWYtNDRmMC1hNDIyLThjZTZjY2JlZjE4ZSIsImRhdGEiOnt9LCJyYW5kb20iOiW64803Z0xB2qQPwOZhXboW-HYAXeoutdVLgcZA4br5QrajZJI1cBcRpGjfiIsCdnxaHkQotKpNWbUYepA. A generalized version of this code with a tutorial to use it can be found in: https://github.com/olfontai/DAS_sensitivity.git. The DAS data, provided in SEGY format, were accessed through the open-source GDR repository (Feigl et al., 2016)

Competing interests

The authors declare no competition of interest.

References

Ajo-Franklin, J. B., Dou, S., Lindsey, N. J., Monga, I., Tracy, C., Robertson, M., Rodriguez Tribaldos, V., Ulrich, C., Freifeld, B., Daley, T., and Li, X. Distributed Acoustic Sensing Using Dark Fiber for Near-Surface Characterization and Broadband Seismic Event Detection. *Scientific Reports*, 9(1):1328, Feb. 2019. doi: 10.1038/s41598-018-36675-8.

Aki, K. and Richards, P. Quantitative Seismology, 2nd Ed. Jan. 2002.

Bakku, S. K. *Fracture characterization from seismic measurements in a borehole*. PhD Thesis, Massachusetts Institute of Technology, 2015. https://dspace.mit.edu/handle/1721.1/97331.

Benioff, H. A linear strain seismograph*. *Bulletin of the Seismological Society of America*, 25(4):283–309, Oct. 1935. doi: 10.1785/BSSA0250040283.

Capdeville, Y. and Sladen, A. DAS sensitivity to heterogeneity scales much smaller than the minimum wavelength. *Seismica*, 3(1), Jan. 2024. doi: 10.26443/seismica.v3i1.1007.

Celli, N. L., Bean, C. J., and O'Brien, G. S. Full-waveform simulation of DAS records, response and cable-ground coupling. *Geophysical Journal International*, 236(1):659–674, Jan. 2024. doi: 10.1093/gji/ggad449.

Currenti, G., Jousset, P., Napoli, R., Krawczyk, C., and Weber, M. On the comparison of strain measurements from fibre optics with a dense seismometer array at Etna volcano (Italy). *Solid Earth*, 12(4):993–1003, Apr. 2021. doi: 10.5194/se-12-993-2021.

Daley, T., Miller, D., Dodds, K., Cook, P., and Freifeld, B. Field testing of modular borehole monitoring with simultaneous distributed acoustic sensing and geophone vertical seismic profiles at Citronelle, Alabama. *Geophysical Prospecting*, 64(5):1318–1334, 2016. doi: 10.1111/1365-2478.12324.

Daley, T. M., Robertson, M., Freifeld, B. M., White, D., Miller, D. E., Herkenhoff, F., and Cocker, J. Simultaneous acquisition of distributed acoustic sensing VSP with multi-mode and single-mode fiber optic cables and 3-component geophones at the Aquistore CO2 storage site. In *SEG Technical Program Expanded Abstracts 2014*, SEG Technical Program Expanded Abstracts, pages 5014–5018. Society of Exploration Geophysicists, Aug. 2014. doi: 10.1190/segam2014-1357.1.

Feigl, K., Reinisch, E., Patterson, J., Jreij, S., Parker, L., Nayak, A., Zeng, X., Cardiff, M., Lord, N. E., Fratta, D., Thurber, C., Wang, H., Robertson, M., Coleman, T., Miller, D. E., Spielman, P., Akerley, J., Kreemer, C., Morency, C., Matzel, E., Trainor-Guitton, W., and Davatzes, N. PoroTomo natural laboratory horizontal and vertical distributed acoustic sensing data, 2016. https://gdr.openei.org/submissions/980. doi: 10.15121/1778858. tex.howpublished: Geothermal Data Repository, University of Wisconsin, https://doi.org/10.15121/1778858.

Feigl, K. L. Material Properties for Brady Hot Springs Nevada USA from PoroTomo Project. Technical Report 1124, USDOE Geothermal Data Repository (United States); Univ. of Wisconsin, Madison, WI (United States), Mar. 2019. https://www.osti.gov/biblio/1501544.

Fichtner, A. and Hofstede, C. A simple algorithm for optimal design in distributed fibre-optic sensing. *Geophysical Journal International*, 233(1):229–233, Apr. 2023. doi: 10.1093/gji/ggac458.

Fichtner, A., Hofstede, C., N. Kennett, B. L., Nymand, N. F., Lauritzen, M. L., Zigone, D., and Eisen, O. Fiber-Optic Airplane Seismology on the Northeast Greenland Ice Stream. *The Seismic Record*, 3(2):125–133, May 2023. doi: 10.1785/0320230004.

Fichtner, A., Walter, F., Brisbourne, A., Booth, A. D., Kendall, J. M., Hudson, T., Paitz, P., and Lipovsky, B. P. Fibre-optic exploration of the cryosphere. *Geophysical Journal International*, 244(2):ggaf489, Feb. 2026. doi: 10.1093/gji/ggaf489.

Han, L., Wong, J., and Bancroft, J. C. Time picking and random noise reduction on microseismic data. 2009.

Hartog, A., Frignet, B., Mackie, D., and Clark, M. Vertical seismic optical profiling on wireline logging cable. *Geophysical Prospecting*, 62(4): 693–701, May 2014. doi: 10.1111/1365-2478.12141.

Hu, M. and Li, Z. DASPy: A Python Toolbox for DAS Seismology. *Seismological Research Letters*, 95(5):3055–3066, July 2024. doi: 10.1785/0220240124.

Hudson, T., Brisbourne, A., Walter, F., Gräff, D., White, R., and Smith, A. Icequake Source Mechanisms for Studying Glacial Sliding. *Journal of Geophysical Research: Earth Surface*, 125, Nov. 2020. doi: 10.1029/2020JF005627.

Hudson, T., Stork, A., Muir, J., and Fichtner, A. Unlocking DAS amplitude information through coherency coupling quantification. *Seismica*, 4(1), Mar. 2025a. doi: 10.26443/seismica.v4i1.1488.

Hudson, T. S., Klaasen, S., Fontaine, O., Bacon, C. A., Jónsdóttir, K., and Fichtner, A. Towards a widely applicable earthquake detection algorithm for fibreoptic and hybrid fibreoptic-seismometer networks. *Geophysical Journal International*, 240(3):1965–1985, Mar. 2025b. doi: 10.1093/gji/ggae459.

Ichinose, G. A., Mellors, R. J., Barno, J. G., and Gok, R. Comparisons Between Array Derived Dynamic Strain Rate (ADDS) and Fiber-Optic Distributed Acoustic Sensing (DAS) Strain Rate. *Journal of Geophysical Research: Solid Earth*, 127(12):e2022JB025101, 2022. doi: 10.1029/2022JB025101.

Jiang, K., Liang, L., Tong, X., Zeng, F., and Hu, X. How the Material Characteristics of Optical Fibers and Soil Influence the Measurement Results of Distributed Acoustic Sensing. *Sensors*, 23(17):7340, Jan. 2023. doi: 10.3390/s23177340.

Jousset, P., Reinsch, T., Ryberg, T., Blanck, H., Clarke, A., Aghayev, R., Hersir, G. P., Henninges, J., Weber, M., and Krawczyk, C. M. Dynamic strain determination using fibre-optic cables allows imaging of seismological and structural features. *Nature Communications*, 9(1):2509,

July 2018. doi: 10.1038/s41467-018-04860-y.

Jousset, P., Currenti, G., Murphy, S., Eibl, E., Caudron, C., Roux, P., Wollin, C., Klaasen, S., Nishimura, T., Fichtner, A., Spica, Z., Marchand, A., and Krawczyk, C. *Fiber optic sensing for volcano monitoring and imaging volcanic processes*. May 2024. doi: 10.31223/X5HM6J.

Kennett, B. The seismic wavefield as seen by distributed acoustic sensing arrays: local, regional and teleseismic sources. *Proceedings of The Royal Society of London*, 478:0812, Feb. 2022. doi: 10.1098/rspa.2021.0812.

Kennett, B. L. N. A Guide to the Seismic Wavefield as seen by DAS. Aug. 2024.

Lindsey, N. J., Martin, E. R., Dreger, D. S., Freifeld, B., Cole, S., James, S. R., Biondi, B. L., and Ajo-Franklin, J. B. Fiber-optic network observations of earthquake wavefields. *Geophysical Research Letters*, 44(23):11,792–11,799, 2017. doi: https://doi.org/10.1002/2017GL075722.

Lindsey, N. J., Rademacher, H., and Ajo-Franklin, J. B. On the Broadband Instrument Response of Fiber-Optic DAS Arrays. *Journal of Geophysical Research: Solid Earth*, 125(2):e2019JB018145, 2020. doi: 10.1029/2019JB018145.

Lior, I., Sladen, A., Rivet, D., Ampuero, J.-P., Hello, Y., Becerril, C., Martins, H. F., Lamare, P., Jestin, C., Tsagkli, S., and Markou, C. On the Detection Capabilities of Underwater Distributed Acoustic Sensing. *Journal of Geophysical Research: Solid Earth*, 126(3):e2020JB020925, 2021. doi: 10.1029/2020JB020925.

Liu, Y. and Schmitt, D. R. The Transition Between the Scale Domains of Ray and Effective Medium Theory and Anisotropy: Numerical Models. *pure and applied geophysics*, 163(7):1327–1349, July 2006. doi: 10.1007/s00024-006-0075-5.

Lokmer, I. and Bean, C. J. Properties of the near-field term and its effect on polarisation analysis and source locations of long-period (LP) and very-long-period (VLP) seismic events at volcanoes. *Journal of Volcanology and Geothermal Research*, 192(1):35–47, Apr. 2010. doi: 10.1016/j.jvolgeores.2010.02.008.

Luo, B., Jin, G., and Stanek, F. Near-field strain in distributed acoustic sensing-based microseismic observation. *Geophysics*, 86(5):P49–P60, Aug. 2021. doi: 10.1190/geo2021-0031.1.

Ma, K.-F., von Specht, S., Kuo, L.-W., Huang, H.-H., Lin, C.-R., Lin, C.-J., Ku, C.-S., Wu, E.-S., Wang, C.-Y., Chang, W.-Y., and Jousset, P. Broadband strain amplification in an asymmetric fault zone observed from borehole optical fiber and core. *Communications Earth & Environment*, 5(1):1–13, July 2024. doi: 10.1038/s43247-024-01558-6.

Martin, E., Lindsey, N., Ajo-Franklin, J., and Biondi, B. Introduction to Interferometry of Fiber-Optic Strain Measurements. pages 111–129. Dec. 2021. doi: 10.1002/9781119521808.ch9.

Martin, E. R., Huot, F., Ma, Y., Cieplicki, R., Cole, S., Karrenbach, M., and Biondi, B. L. A Seismic Shift in Scalable Acquisition Demands New Processing: Fiber-Optic Seismic Signal Retrieval in Urban Areas with Unsupervised Learning for Coherent Noise Removal. *IEEE Signal Processing Magazine*, 35(2):31–40, Mar. 2018. doi: 10.1109/MSP.2017.2783381.

Muir, J. B. and Zhan, Z. Wavefield-based evaluation of DAS instrument response and array design. *Geophysical Journal International*, 229 (1):21–34, Apr. 2022. doi: 10.1093/gji/ggab439.

Nakano, M., Ichihara, M., Suetsugu, D., Ohminato, T., Ono, S., Vaiomounga, R., Kula, T., and Shinohara, M. Monitoring volcanic activity with distributed acoustic sensing using the Tongan seafloor telecommunications cable. *Earth, Planets and Space*, 76(1):25, Feb. 2024. doi: 10.1186/s40623-024-01972-2.

Nishimura, T., Emoto, K., Nakahara, H., Miura, S., Yamamoto, M., Sugimura, S., Ishikawa, A., and Kimura, T. Source location of volcanic earthquakes and subsurface characterization using fiber-optic cable and distributed acoustic sensing system. *Scientific Reports*, 11(1): 6319, Mar. 2021. doi: 10.1038/s41598-021-85621-8.

Noe, S., Tuinstra, K. B., Klaasen, S., Krischer, L., and Fichtner, A. Theoretical background for full-waveform inversion with distributed acoustic sensing and integrated strain sensing. *Geophysical Journal International*, 244(1):ggaf406, Jan. 2026. doi: 10.1093/gji/ggaf406.

Paitz, P., Edme, P., Gräff, D., Walter, F., Doetsch, J., Chalari, A., Schmelzbach, C., and Fichtner, A. Empirical Investigations of the Instrument Response for Distributed Acoustic Sensing (DAS) across 17 Octaves. *Bulletin of the Seismological Society of America*, 111(1):1–10, Oct. 2020. doi: 10.1785/0120200185.

Rawlinson, N., Hauser, J., and Sambridge, M. Seismic ray tracing and wavefront tracking in laterally heterogeneous media. In Dmowska, R., editor, *Advances in Geophysics*, volume 49, pages 203–273. Elsevier, Jan. 2008. doi: 10.1016/S0065-2687(07)49003-3.

Siler, D. L. and Pepin, J. D. 3-D Geologic Controls of Hydrothermal Fluid Flow at Brady geothermal field, Nevada, USA. *Geothermics*, 94: 102112, July 2021. doi: 10.1016/j.geothermics.2021.102112.

Vantassel, J. P., Cox, B. R., Hubbard, P. G., Yust, M., Menq, F., Spikes, K., and Fratta, D. Effectiveness of Distributed Acoustic Sensing for Acquiring Surface Wave Dispersion Data Using Multichannel Analysis of Surface Waves. In Wang, L., Zhang, J.-M., and Wang, R., editors, *Proceedings of the 4th International Conference on Performance Based Design in Earthquake Geotechnical Engineering (Beijing 2022)*, pages 1000–1008, Cham, 2022. Springer International Publishing. doi: 10.1007/978-3-031-11898-2$_7$7.

Vera Rodriguez, I. and Wuestefeld, A. Strain microseismics: Radiation patterns, synthetics, and moment tensor resolvability with distributed acoustic sensing in isotropic media. *Geophysics*, 85(3):KS101–KS114, Apr. 2020. doi: 10.1190/geo2019-0373.1.

Walter, F., Gräff, D., Lindner, F., Paitz, P., Köpfli, M., Chmiel, M., and Fichtner, A. Distributed acoustic sensing of microseismic sources and wave propagation in glaciated terrain. *Nature Communications*, 11(1):2436, May 2020. doi: 10.1038/s41467-020-15824-6.

Wang, H. F., Zeng, X., Miller, D. E., Fratta, D., Feigl, K. L., Thurber, C. H., and Mellors, R. J. Ground motion response to an ML 4.3 earthquake using co-located distributed acoustic sensing and seismometer arrays. *Geophysical Journal International*, 213(3):2020–2036, June 2018. doi: 10.1093/gji/ggy102.

White, M. C. A., Fang, H., Nakata, N., and Ben-Zion, Y. PyKonal: A Python Package for Solving the Eikonal Equation in Spherical and Cartesian Coordinates Using the Fast Marching Method. *Seismological Research Letters*, 91(4):2378–2389, June 2020. doi: 10.1785/0220190318.

Xie, T., Zhang, C.-C., Shi, B., Li, J.-P., and Zhang, T.-Y. Could fiber strains affect DAS amplitude response? *Measurement*, 189:110428, Feb. 2022. doi: 10.1016/j.measurement.2021.110428.

Yin, J., Soto, M. A., Ramírez, J., Kamalov, V., Zhu, W., Husker, A., and Zhan, Z. Real-Data Testing of Distributed Acoustic Sensing for Offshore Earthquake Early Warning. *The Seismic Record*, 3(4):269–277, Oct. 2023. doi: 10.1785/0320230018.

Zeng, X., Thurber, C., Wang, H., Fratta, D., Matzel, E., and Team, P. High-resolution shallow structure revealed with ambient noise tomography on a dense array. Feb. 2017.

Supplementary Materials: Understanding fiber-optic sensitivity to a wavefield A framework to separate site amplification from orientation effects

1 Linear fiber sensitivity equations demonstration

In these demonstrations, we derive the expression for the strain rate, along the fiber direction, generated by a plane wave propagating in the direction :

$$[\cos(\varphi_{ray})\cos(\theta_{ray}),\ \sin(\varphi_{ray})\cos(\theta_{ray}),\ \sin(\theta_{ray})].$$

Here, φ denotes the azimuth and θ the dip, both defined with respect to the trigonometric convention.

We begin with a set of polarization vectors that describe the displacement for each wave type. Taking the time derivative yields particle velocity. Then applying a spatial derivative gives the strain rate. The gauge length effect is accounted for by averaging the strain rate over a linear segment aligned with the fiber direction.

In the second part, when considering looped gauge lengths, the averaging is performed over all azimuths or dips, depending on the orientation of the loop.

1.0.1 Abbreviation Summary

- A: Amplitude
- $\psi(x, y, z, t)$: Oscillatory factor for P- and S-waves, expressed as

$$e^{ik(ct - x\cos(\varphi_{ray})\cos(\theta_{ray}) - y\sin(\varphi_{ray})\cos(\theta_{ray}) - z\sin(\theta_{ray}))}$$

- $\dot{\epsilon}_{xx'}$: Strain rate in the xx' direction, rotated into the fiber's direction
- φ_{ray}: Ray azimuth
- θ_{ray}: Ray dip
- φ_{DAS}: DAS azimuth
- θ_{DAS}: DAS dip
- R: Gauge length loop radius
- g: Gauge length

1.1 rotational matrix and strain tensor in xx' direction

Creation of a rotational matrix for the xx component of the strain tensor for all azimuth (z-axis rotation), and all dip (Y-axis rotation)

$$\begin{bmatrix} \cos(\theta_{DAS}) & 0 & \sin(\theta_{DAS}) \\ 0 & 1 & 0 \\ -\sin(\theta_{DAS}) & 0 & \cos(\theta_{DAS}) \end{bmatrix} * \begin{bmatrix} \cos(\varphi_{DAS}) & \sin(\varphi_{DAS}) & 0 \\ -\sin(\varphi_{DAS}) & \cos(\varphi_{DAS}) & 0 \\ 0 & 0 & 1 \end{bmatrix}$$
$$= \begin{bmatrix} \cos(\varphi_{DAS})\cos(\theta_{DAS}) & \sin(\varphi_{DAS})\cos(\theta_{DAS}) & \sin(\theta_{DAS}) \\ -\sin(\varphi_{DAS}) & \cos(\varphi_{DAS}) & 0 \\ -\sin(\theta_{DAS})\cos(\varphi_{DAS}) & \cos(\theta_{DAS}) & \cos(\theta_{DAS}) \end{bmatrix}$$

Rotation of the ϵ_{xx} component of the strain tensor:

$$M.\epsilon.M^T$$

$$\epsilon_{xx'} = \begin{bmatrix} \cos(\varphi_{DAS})\cos(\theta_{DAS}) & \sin(\varphi_{DAS})\cos(\theta_{DAS}) & \sin(\theta_{DAS}) \end{bmatrix} . \begin{bmatrix} \epsilon_{xx} & \epsilon_{xy} & \epsilon_{xz} \\ \epsilon_{yx} & \epsilon_{yy} & \epsilon_{yz} \\ \epsilon_{zx} & \epsilon_{zy} & \epsilon_{zz} \end{bmatrix} . \begin{bmatrix} \cos(\varphi_{DAS})\cos(\theta_{DAS}) \\ \sin(\varphi_{DAS})\cos(\theta_{DAS}) \\ \sin(\theta_{DAS}) \end{bmatrix}$$

using the conservation of angular momentum ($\epsilon_{ij} = \epsilon_{ji}$) :

$$\begin{aligned} \epsilon xx' =& \cos(\varphi_{DAS})^2 \cos(\theta_{DAS})^2 \epsilon_{xx} + \sin(2\varphi_{DAS}) \cos(\theta_{DAS})^2 \epsilon_{yx} + \sin(2\theta_{DAS}) \cos(\varphi_{DAS}) \epsilon_{xz} \\ &+ \sin(\varphi_{DAS})^2 \cos(\theta_{DAS})^2 \epsilon_{yy} + \sin(2\theta_{DAS}) \sin(\varphi_{DAS}) \epsilon_{zy} + \sin(\theta_{DAS})^2 \epsilon zz \end{aligned} \tag{1}$$

1.2 P waves

Starting from the polarization specific displacement vector (u):

$$u = \begin{bmatrix} A\cos(\varphi_{ray})\cos(\theta_{ray})\psi(x,y,z,t) \\ A\sin(\varphi_{ray})\cos(\theta_{ray})\psi(x,y,z,t) \\ A\sin(\theta_{ray})\psi(x,y,z,t) \end{bmatrix}$$

$$u_{x'} = \begin{bmatrix} \cos(\varphi_{DAS})\cos(\theta_{DAS}) & \sin(\varphi_{DAS})\cos(\theta_{DAS}) & \sin(\theta_{DAS}) \\ -\sin(\varphi_{DAS}) & \cos(\varphi_{DAS}) & 0 \\ -\sin(\theta_{DAS})\cos(\varphi_{DAS}) & \cos(\theta_{DAS}) & \cos(\theta_{DAS}) \end{bmatrix} \begin{bmatrix} A\cos(\varphi_{ray})\cos(\theta_{ray})\psi(x,y,z,t) \\ A\sin(\varphi_{ray})\cos(\theta_{ray})\psi(x,y,z,t) \\ A\sin(\theta_{ray})\psi(x,y,z,t) \end{bmatrix}$$
$$= \boxed{A(\cos(\theta_{DAS})\cos(\theta_{ray})\cos(\varphi_{ray} - \varphi_{DAS}) + \sin(\theta_{ray})\sin(\theta_{DAS}))\psi(x,y,z,t)}$$

We apply a time derivative to get velocity ($\dot{u}$):

$$\dot{u} = \begin{bmatrix} Akic\cos(\varphi_{ray})\cos(\theta_{ray})\psi(x,y,z,t) \\ Akic\sin(\varphi_{ray})\cos(\theta_{ray})\psi(x,y,z,t) \\ Akic\sin(\theta_{ray})\psi(x,y,z,t) \end{bmatrix}$$

$$\dot{u}_{x'} = \frac{\delta u_{x'}}{\delta t} = \boxed{Aik(\cos(\theta_{DAS})\cos(\theta_{ray})\cos(\varphi_{ray} - \varphi_{DAS}) + \sin(\theta_{ray})\sin(\theta_{DAS}))\psi(x,y,z,t)}$$

Then a spatial partial derivative to get the component of the strain tensor in the ij direction ($\dot{\epsilon}_{ij}$):

$$\begin{aligned} \dot{\epsilon}_{xx} &= k^2 cA\cos(\varphi_{ray})^2\cos(\theta_{ray})^2\psi(x,y,z,t) \\ \dot{\epsilon}_{xy} &= \tfrac{k^2cA}{2}\sin(2\varphi_{ray})\psi(x,y,z,t) \\ \dot{\epsilon}_{xz} &= \tfrac{k^2cA}{2}\cos(\varphi_{ray})\sin(2\theta_{ray})\psi(x,y,z,t) \\ \dot{\epsilon}_{yx} &= \tfrac{k^2cA}{2}\sin(2\varphi_{ray})\cos(\theta_{ray})^2\psi(x,y,z,t) \\ \dot{\epsilon}_{yy} &= k^2 cA\sin(\varphi_{ray})^2\cos(\theta_{ray})^2\psi(x,y,z,t) \end{aligned}$$

$$\begin{aligned} \dot{\epsilon}_{yz} &= \tfrac{k^2cA}{2}\sin(\varphi_{ray})\sin(2\theta_{ray})\psi(x,y,z,t) \\ \dot{\epsilon}_{zx} &= \tfrac{k^2cA}{2}\cos(\varphi_{ray})\sin(2\theta_{ray})\psi(x,y,z,t) \\ \dot{\epsilon}_{zy} &= \tfrac{k^2cA}{2}\sin(\varphi_{ray})\sin(2\theta_{ray})\psi(x,y,z,t) \\ \dot{\epsilon}_{zz} &= k^2 cA\sin(\theta_{ray})^2\psi(x,y,z,t) \end{aligned}$$

Then from equation 1 we get the strain rate in direction xx':

$$
\begin{aligned}
\dot{\epsilon}_{xx'} =& k^2 cA(\cos(\varphi_{DAS})^2 \cos(\theta_{DAS})^2 \cos(\varphi_{ray})^2 \cos(\theta_{ray})^2 + \cos(\varphi_{DAS}) \sin(\varphi_{DAS}) \cos(\theta_{DAS})^2 \\
& \sin(2\varphi_{ray}) \cos(\theta_{ray})^2 + \cos(\varphi_{DAS}) \cos(\theta_{DAS}) \sin(\theta_{DAS}) \cos(\varphi_{ray}) \sin(2\theta_{ray}) + \sin(\varphi_{DAS})^2 \\
& \cos(\theta_{DAS})^2 \sin(\varphi_{ray})^2 \cos(\theta_{ray})^2 + \sin(\varphi_{DAS}) \sin(\theta_{DAS}) \cos(\theta_{DAS}) \sin(\varphi_{ray}) \sin(2\theta_{ray}) \\
& + \sin(\theta_{DAS})^2 \sin(\theta_{ray})^2) \psi(x, y, z, t) \\
=& k^2 cA(\cos(\theta_{DAS})^2 \cos(\theta_{ray})^2 (\cos(\varphi_{ray})^2 \cos(\varphi_{DAS})^2 + \frac{\sin(2\varphi_{DAS}) \sin(2\varphi_{ray})}{2} \\
& + \sin(\varphi_{DAS})^2 \sin(\varphi_{ray})^2) + 2\cos(\theta_{ray}) \sin(\theta_{ray}) \cos(\theta_{DAS}) \sin(\theta_{DAS}) (\cos(\varphi_{DAS}) \cos(\varphi_{ray}) \\
& + \sin(\varphi_{DAS}) \sin(\varphi_{ray})) + \sin(\theta_{DAS})^2 \sin(\theta_{ray})^2) \psi(x, y, z, t) \\
=& k^2 cA(\cos(\theta_{DAS})^2 \cos(\theta_{ray})^2 \cos(\varphi_{DAS} - \varphi_{ray})^2 + 2\sin(\theta_{ray}) \cos(\theta_{ray}) \cos(\theta_{DAS}) \\
& \sin(\theta_{DAS}) \cos(\varphi_{DAS} - \varphi_{ray}) + \sin(\theta_{DAS})^2 \sin(\theta_{ray})^2) \psi(x, y, z, t) \\
=& \boxed{k^2 cA(\cos(\theta_{DAS}) \cos(\theta_{ray}) \cos(\varphi_{DAS} - \varphi_{ray}) + \sin(\theta_{DAS}) \sin(\theta_{ray}))^2 \psi(x, y, z, t)}
\end{aligned}
$$

To consider the gauge length effect, we average the strain over a linear segment of direction.

$[\cos(\varphi_{DAS})\cos(\theta_{DAS}), \sin(\varphi_{DAS})\cos(\theta_{DAS}), \sin(\theta_{DAS})]$:

$$
\begin{aligned}
\dot{\epsilon}_{xx'g} =& \frac{1}{g}\int_{\frac{+g}{2}}^{\frac{-g}{2}} \dot{\epsilon}_{xx'}(x + v\cos(\varphi_{DAS})\cos(\theta_{DAS}), y + v\sin(\varphi_{DAS})\cos(\theta_{DAS}), z + v\sin(\theta_{DAS}), t)dv \\
=& \frac{k^2cA}{g}(\cos(\theta_{DAS})\cos(\theta_{ray})\cos(\varphi_{DAS} - \varphi_{ray}) + \sin(\theta_{DAS})\sin(\theta_{ray}))^2 \\
& \int_{\frac{+g}{2}}^{\frac{-g}{2}} e^{ik(ct-(x+v\cos(\varphi_{DAS})\cos(\theta_{DAS}))\cos(\varphi_{ray})\cos(\theta_{ray})-(y+v\sin(\varphi_{DAS})\cos(\theta_{DAS}))\sin(\varphi_{ray})\cos(\theta_{ray})-(z+v\sin(\theta_{DAS}))\sin(\theta_{ray})}dv \\
=& \frac{k^2cA}{g}(\cos(\theta_{DAS})\cos(\theta_{ray})\cos(\varphi_{DAS} - \varphi_{ray}) + \sin(\theta_{DAS})\sin(\theta_{ray}))^2 \\
& \int_{\frac{+g}{2}}^{\frac{-g}{2}} e^{ik(ct-x\cos(\varphi_{ray})\cos(\theta_{ray})-y\sin(\varphi_{ray})\cos(\theta_{ray})-z\sin(\theta_{ray}))} \\
& e^{-ik(v\cos(\varphi_{DAS})\cos(\theta_{DAS})\cos(\varphi_{ray})\cos(\theta_{ray})-v\sin(\varphi_{DAS})\cos(\theta_{DAS})\sin(\varphi_{ray})\cos(\theta_{ray})-v\sin(\theta_{DAS})\sin(\theta_{ray}))}dv \\
=& \frac{k^2cA}{g}(\cos(\theta_{DAS})\cos(\theta_{ray})\cos(\varphi_{DAS} - \varphi_{ray}) + \sin(\theta_{DAS})\sin(\theta_{ray}))^2\psi(x,y,z,t) \\
& [\frac{e^{-ikv(\cos(\varphi_{DAS})\cos(\theta_{DAS})\cos(\varphi_{ray})\cos(\theta_{ray})+\sin(\varphi_{DAS})\cos(\theta_{DAS})\sin(\varphi_{ray})\cos(\theta_{ray})+\sin(\theta_{DAS})\sin(\theta_{ray}))}}{ik(\cos(\varphi_{DAS})\cos(\theta_{DAS})\cos(\varphi_{ray})\cos(\theta_{ray}) + \sin(\varphi_{DAS})\cos(\theta_{DAS})\sin(\varphi_{ray})\cos(\theta_{ray}) + \sin(\theta_{DAS})\sin(\theta_{ray}))}]_{\frac{+g}{2}}^{\frac{-g}{2}} \\
=& \frac{k^2cA}{kg}\frac{(\cos(\theta_{DAS})\cos(\theta_{ray})\cos(\varphi_{DAS} - \varphi_{ray}) + \sin(\theta_{DAS})\sin(\theta_{ray}))^2}{(\cos(\theta_{DAS})\cos(\theta_{ray})\cos(\varphi_{DAS} - \varphi_{ray}) + \sin(\theta_{DAS})\sin(\theta_{ray})}\psi(x,y,z,t) \\
& [\frac{e^{-ikv((\cos(\theta_{DAS})\cos(\theta_{ray})\cos(\varphi_{DAS}-\varphi_{ray})+\sin(\theta_{DAS})\sin(\theta_{ray}))}}{i}]_{\frac{+g}{2}}^{\frac{-g}{2}} \\
=& \frac{kcA}{g}(\cos(\theta_{DAS})\cos(\theta_{ray})\cos(\varphi_{DAS} - \varphi_{ray}) + \sin(\theta_{DAS})\sin(\theta_{ray}))\psi(x,y,z,t) \\
& [\frac{e^{-ikv((\cos(\theta_{DAS})\cos(\theta_{ray})\cos(\varphi_{DAS}-\varphi_{ray})+\sin(\theta_{DAS})\sin(\theta_{ray}))}}{i}]_{\frac{+g}{2}}^{\frac{-g}{2}} \\
=& \frac{kcA}{g}(\cos(\theta_{DAS})\cos(\theta_{ray})\cos(\varphi_{DAS} - \varphi_{ray}) + \sin(\theta_{DAS})\sin(\theta_{ray}))\psi(x,y,z,t) \\
& 2[\frac{e^{-ik\frac{-g}{2}(\cos(\theta_{DAS})\cos(\theta_{ray})\cos(\varphi_{DAS}-\varphi_{ray})+\sin(\theta_{DAS})\sin(\theta_{ray}))}}{2i} \\
& - \frac{e^{-ik\frac{+g}{2}(\cos(\theta_{DAS})\cos(\theta_{ray})\cos(\varphi_{DAS}-\varphi_{ray})+\sin(\theta_{DAS})\sin(\theta_{ray}))}}{2i}] \\
=& \boxed{\begin{aligned}&\frac{2kcA}{g}(\cos(\theta_{DAS})\cos(\theta_{ray})\cos(\varphi_{DAS} - \varphi_{ray}) + \sin(\theta_{DAS})\sin(\theta_{ray})) \\ &\times \sin\left(\frac{kg}{2}(\cos(\theta_{DAS})\cos(\theta_{ray})\cos(\varphi_{DAS} - \varphi_{ray}) + \sin(\theta_{DAS})\sin(\theta_{ray}))\right)\psi(x,y,z,t)\end{aligned}}
\end{aligned}
\tag{2}
$$

1.3 SH waves

Starting from the polarization specific displacement vector (u):

$$
u = \begin{bmatrix} A\sin(\varphi_{ray})\psi(x,y,z,t) \\ A\cos(\varphi_{ray})\psi(x,y,z,t) \\ 0 \end{bmatrix}
$$

$$
\begin{aligned}
u_{x'} =& \begin{bmatrix} \cos(\varphi_{DAS})\cos(\theta_{DAS}) & \sin(\varphi_{DAS})\cos(\theta_{DAS}) & \sin(\theta_{DAS}) \\ -\sin(\varphi_{DAS}) & \cos(\varphi_{DAS}) & 0 \\ -\sin(\theta_{DAS})\cos(\varphi_{DAS}) & \cos(\theta_{DAS}) & \cos(\theta_{DAS}) \end{bmatrix} \begin{bmatrix} A\sin(\varphi_{ray})\psi(x,y,z,t) \\ A\cos(\varphi_{ray})\psi(x,y,z,t) \\ 0 \end{bmatrix} \\
=& \boxed{A\cos(\theta_{DAS})\sin(\varphi_{ray} - \varphi_{DAS})\psi(x,y,z,t)}
\end{aligned}
$$

We apply a time derivative to get velocity ($\dot{u}$):

$$u = \begin{bmatrix} Akic\sin(\varphi_{ray})\,\psi(x,y,z,t) \\ Akic\cos(\varphi_{ray})\,\psi(x,y,z,t) \\ 0 \end{bmatrix}$$

$$\dot{u}_{x'} = \frac{\delta \dot{u}}{\delta t} = \boxed{Akic\cos(\theta_{DAS})\sin(\varphi_{ray}-\varphi_{DAS})\,\psi(x,y,z,t)}$$

Then a spatial partial derivative to get the component of the strain tensor in the ij direction ($\dot{\epsilon}_{ij}$):

$$\begin{aligned}
\dot{\epsilon}_{xx} &= \frac{k^2cA}{2}\sin(2\varphi_{ray})\cos(\theta_{ray})\,\psi(x,y,z,t) \\
\dot{\epsilon}_{xy} &= k^2cA\sin(\varphi_{ray})^2\cos(\theta_{ray})\,\psi(x,y,z,t) \\
\dot{\epsilon}_{xz} &= k^2cA\sin(\varphi_{ray})\sin(\theta_{ray})\,\psi(x,y,z,t) \\
\dot{\epsilon}_{yx} &= -k^2cA\cos(\varphi_{ray})^2\cos(\theta_{ray})\,\psi(x,y,z,t) \\
\dot{\epsilon}_{yy} &= \frac{-k^2cA}{2}\sin(2\varphi_{ray})\cos(\theta_{ray})\,\psi(x,y,z,t)
\end{aligned}
\qquad
\begin{aligned}
\dot{\epsilon}_{yz} &= -k^2cA\cos(\varphi_{ray})\sin(\theta_{ray})\,\psi(x,y,z,t) \\
\dot{\epsilon}_{zx} &= 0 \\
\dot{\epsilon}_{zy} &= 0 \\
\dot{\epsilon}_{zz} &= 0
\end{aligned}$$

Then from equation 1 we get the strain rate in direction xx':

$$\begin{aligned}
\dot{\epsilon}_{xx'} =& ck^2A\Big(\frac{\cos(\varphi_{DAS})^2\cos(\theta_{DAS})^2\sin(2\varphi_{ray})\cos(\theta_{ray})}{2} + \\
& \frac{\sin(2\varphi_{DAS})\cos(\theta_{DAS})^2\cos(\theta_{ray})\left(\sin(\varphi_{ray})^2-\cos(\varphi_{ray})^2\right)}{2} + \frac{\sin(2\theta_{DAS})\cos(\varphi_{DAS})\sin(\varphi_{ray})\sin(\theta_{ray})}{2} \\
& - \frac{\sin(\varphi_{DAS})^2\cos(\theta_{DAS})^2\sin(2\varphi_{ray})\cos(\theta_{ray})}{2} - \frac{\sin(2\theta_{DAS})\sin(\varphi_{DAS})\cos(\varphi_{ray})\sin(\theta_{ray})}{2}\Big)\psi(x,y,z,t) \\
=& \frac{ck^2A}{2}\big(\sin(2\varphi_{ray})\cos(\theta_{ray})\cos(\theta_{DAS})^2\left(\cos(\varphi_{DAS})^2-\sin(\varphi_{DAS})^2\right) \\
& - \sin(2\varphi_{DAS})\cos(\theta_{DAS})^2\cos(\theta_{ray})\cos(2\varphi_{ray}) + \sin(2\theta_{DAS})\sin(\theta_{ray})\left(\cos(\varphi_{DAS})\sin(\varphi_{ray})\right) \\
& - \sin(\varphi_{DAS})\cos(\varphi_{ray})\big)\big)\psi(x,y,z,t) \\
=& \frac{ck^2A}{2}\big(\sin(2\varphi_{ray})\cos(\theta_{ray})\cos(\theta_{DAS})^2\cos(2\varphi_{DAS}) - \sin(2\varphi_{DAS})\cos(\theta_{DAS})^2\cos(\theta_{ray})\cos(2\varphi_{ray}) \\
& + \sin(2\theta_{DAS})\sin(\theta_{ray})\sin(\varphi_{ray}-\varphi_{DAS})\big)\psi(x,y,z,t) \\
=& \frac{ck^2A}{2}\big(\cos(\theta_{ray})\cos(\theta_{DAS})^2\left(\sin(2\varphi_{ray})\cos(2\varphi_{DAS}) - \sin(2\varphi_{DAS})\cos(2\varphi_{ray})\right) \\
& + \sin(2\theta_{DAS})\sin(\theta_{ray})\sin(\varphi_{ray}-\varphi_{DAS})\big)\psi(x,y,z,t) \\
=& \frac{ck^2A}{2}\big(\cos(\theta_{ray})\cos(\theta_{DAS})^2\sin(2(\varphi_{ray}-\varphi_{DAS})) + \sin(2\theta_{DAS})\sin(\theta_{ray})\sin(\varphi_{ray}-\varphi_{DAS})\big)\psi(x,y,z,t) \\
=& \boxed{ck^2A\sin(\varphi_{ray}-\varphi_{DAS})\cos(\theta_{DAS})\left(\cos(\theta_{ray})\cos(\theta_{DAS})\cos(\varphi_{ray}-\varphi_{DAS})+\sin(\theta_{DAS})\sin(\theta_{ray})\right)\psi(x,y,z,t)}
\end{aligned}$$

To consider the gauge length effect, we average the strain over a linear segment of direction

$[\cos(\varphi_{DAS})\cos(\theta_{DAS}), \sin(\varphi_{DAS})\cos(\theta_{DAS}), \sin(\theta_{DAS})]$ using some steps from 2:

$$
\begin{aligned}
\dot{\epsilon}_{xx'g} =& \frac{1}{g}\int_{\frac{+g}{2}}^{\frac{-g}{2}} \dot{\epsilon}_{xx'}(x + v\cos(\varphi_{DAS})\cos(\theta_{DAS}), y + v\sin(\varphi_{DAS})\cos(\theta_{DAS}), z + v\sin(\theta_{DAS}), t)dv \\
=& \frac{k^2 cA}{g}\sin(\varphi_{ray} - \varphi_{DAS})\cos(\theta_{DAS})(\cos(\theta_{ray})\cos(\theta_{DAS})\cos(\varphi_{ray} - \varphi_{DAS}) + \sin(\theta_{DAS})\sin(\theta_{ray})) \\
& \int_{\frac{+g}{2}}^{\frac{-g}{2}} e^{ik(ct-(x+v\cos(\varphi_{DAS})\cos(\theta_{DAS}))\cos(\varphi_{ray})\cos(\theta_{ray})-(y+v\sin(\varphi_{DAS})\cos(\theta_{DAS}))\sin(\varphi_{ray})\cos(\theta_{ray})-(z+v\sin(\theta_{DAS}))\sin(\theta_{ray})} dv \\
=& \frac{ck^2 A}{kg}\sin(\varphi_{ray} - \varphi_{DAS})\cos(\theta_{DAS})\frac{(\cos(\theta_{ray})\cos(\theta_{DAS})\cos(\varphi_{ray} - \varphi_{DAS}) + \sin(\theta_{DAS})\sin(\theta_{ray}))}{(\cos(\theta_{ray})\cos(\theta_{DAS})\cos(\varphi_{ray} - \varphi_{DAS}) + \sin(\theta_{DAS})\sin(\theta_{ray}))} \\
& sin(\frac{kg}{2}(\cos(\theta_{DAS})\cos(\theta_{ray})\cos(\varphi_{DAS} - \varphi_{ray}) + \sin(\theta_{DAS})\sin(\theta_{ray})))\psi(x, y, z, t) \\
=& \boxed{\frac{2ckA}{g}\sin(\varphi_{ray} - \varphi_{DAS})\cos(\theta_{DAS})\, sin(\frac{kg}{2}(\cos(\theta_{DAS})\cos(\theta_{ray})\cos(\varphi_{DAS} - \varphi_{ray}) + \sin(\theta_{DAS})\sin(\theta_{ray})))\psi(x, y, z, t)}
\end{aligned}
$$

1.4 SV waves

Starting from the polarization specific displacement vector (u):

$$
u = \begin{bmatrix} A\cos(\varphi_{ray})\sin(\theta_{ray})\,\psi(x, y, z, t) \\ A\sin(\varphi_{ray})\sin(\theta_{ray})\,\psi(x, y, z, t) \\ A\cos(\theta_{ray})\,\psi(x, y, z, t) \end{bmatrix}
$$

$$
\begin{aligned}
u_{x'} =& \begin{bmatrix} \cos(\varphi_{DAS})\cos(\theta_{DAS}) & \sin(\varphi_{DAS})\cos(\theta_{DAS}) & \sin(\theta_{DAS}) \\ -\sin(\varphi_{DAS}) & \cos(\varphi_{DAS}) & 0 \\ -\sin(\theta_{DAS})\cos(\varphi_{DAS}) & \cos(\theta_{DAS}) & \cos(\theta_{DAS}) \end{bmatrix} \begin{bmatrix} A\cos(\varphi_{ray})\sin(\theta_{ray})\,\psi(x, y, z, t) \\ A\sin(\varphi_{ray})\sin(\theta_{ray})\,\psi(x, y, z, t) \\ A\cos(\theta_{ray})\,\psi(x, y, z, t) \end{bmatrix} \\
=& \boxed{A(\cos(\theta_{DAS})\sin(\theta_{ray})\cos(\varphi_{DAS} - \varphi_{ray}) + \sin(\theta_{DAS})\cos(\theta_{ray}))\psi(x, y, z, t)}
\end{aligned}
$$

We apply a time derivative to get velocity ($\dot{u}$):

$$
\dot{u} = \begin{bmatrix} Akic\cos(\varphi_{ray})\sin(\theta_{ray})\,\psi(x, y, z, t) \\ Akic\sin(\varphi_{ray})\sin(\theta_{ray})\,\psi(x, y, z, t) \\ Akic\cos(\theta_{ray})\,\psi(x, y, z, t) \end{bmatrix}
$$

$$
\dot{u}_{x'} = \frac{\delta \dot{u}}{\delta t} = \boxed{Akic(\cos(\theta_{DAS})\sin(\theta_{ray})\cos(\varphi_{DAS} - \varphi_{ray}) + \sin(\theta_{DAS})\cos(\theta_{ray}))\psi(x, y, z, t)}
$$

Then a spatial partial derivative to get the component of the strain tensor in the ij direction ($\dot{\epsilon}_{ij}$):

$$
\begin{aligned}
\dot{\epsilon}_{xx} &= \frac{-k^2 cA}{2}\cos(\varphi_{ray})^2\sin(2\theta_{ray})\,\psi(x, y, z, t) \\
\dot{\epsilon}_{xy} &= \frac{-k^2 cA}{4}\sin(2\varphi_{ray})\sin(2\theta_{ray})\,\psi(x, y, z, t) \\
\dot{\epsilon}_{xz} &= -k^2 cA\cos(\varphi_{ray})\sin(\theta_{ray})^2\,\psi(x, y, z, t) \\
\dot{\epsilon}_{yx} &= \frac{-k^2 cA}{4}\sin(2\varphi_{ray})\sin(2\theta_{ray})\,\psi(x, y, z, t) \\
\dot{\epsilon}_{yy} &= \frac{-k^2 cA}{2}\sin(2\varphi_{ray})\cos(\theta_{ray})\,\psi(x, y, z, t) \\
\dot{\epsilon}_{yz} &= -k^2 cA\sin(\varphi_{ray})\sin(\theta_{ray})^2\,\psi(x, y, z, t) \\
\dot{\epsilon}_{zx} &= k^2 cA\cos(\varphi_{ray})\cos(\theta_{ray})^2\,\psi(x, y, z, t) \\
\dot{\epsilon}_{zy} &= k^2 cA\sin(\varphi_{ray})\cos(\theta_{ray})^2\,\psi(x, y, z, t) \\
\dot{\epsilon}_{zz} &= \frac{k^2 cA}{2}\sin(2\theta_{ray})\,\psi(x, y, z, t)
\end{aligned}
$$

Then from equation 1 we get the strain rate in direction xx':

$$
\begin{aligned}
\dot{\epsilon}_{xx'} =& k^2 cA\Big(\frac{-\cos(\varphi_{DAS})^2\cos(\theta_{DAS})^2\cos(\varphi_{ray})^2\sin(2\theta_{ray})}{2} - \frac{\sin(\varphi_{DAS})\cos(\varphi_{DAS})\cos(\theta_{DAS})^2\sin(2\varphi_{ray})\sin(2\theta_{ray})}{2} \\
&+ \cos(\varphi_{DAS})\cos(\theta_{DAS})\sin(\theta_{DAS})\left(-\cos(\varphi_{ray})\sin(\theta_{ray})^2 + \cos(\varphi_{ray})\cos(\theta_{ray})^2\right) \\
&- \frac{\sin(\varphi_{DAS})^2\cos(\theta_{DAS})^2\sin(\varphi_{ray})^2\sin(2\theta_{ray})}{2} + \cos(\theta_{DAS})\sin(\theta_{DAS})\sin(\varphi_{DAS})\left(-\sin(\varphi_{ray})\sin(\theta_{ray})^2\right. \\
&\left.+ \sin(\varphi_{ray})\cos(\theta_{ray})^2\right) + \frac{\sin(\theta_{DAS})^2\sin(2\theta_{ray})}{2}\Big)\psi(x,y,z,t) \\
=& \frac{k^2 cA}{2}\Big(-\cos(\varphi_{DAS})^2\cos(\theta_{DAS})^2\cos(\varphi_{ray})^2\sin(2\theta_{ray}) - \frac{\sin(2\varphi_{DAS})\cos(\theta_{DAS})^2\sin(2\varphi_{ray})\sin(2\theta_{ray})}{2} \\
&+ \cos(\varphi_{DAS})\sin(2\theta_{DAS})\cos(\varphi_{ray})\cos(2\theta_{ray}) - \sin(\varphi_{DAS})^2\cos(\theta_{DAS})^2\sin(\varphi_{ray})^2\sin(2\theta_{ray}) \\
&+ \sin(2\theta_{DAS})\sin(\varphi_{DAS})\sin(\varphi_{ray})\cos(2\theta_{ray}) + \sin(\theta_{DAS})^2\sin(2\theta_{ray})\Big)\psi(x,y,z,t) \\
=& \frac{k^2 cA}{2}\Big(-\cos(\theta_{DAS})^2\sin(2\theta_{ray})\left(\cos(\varphi_{DAS})^2\cos(\varphi_{ray})^2 + \frac{\sin(2\theta 1)\sin(2\varphi_{ray})}{2} + \sin(\varphi_{DAS})^2\sin(\varphi_{ray})^2\right) \\
&+ \sin(2\theta_{DAS})\cos(2\theta_{DAS})\left(\cos(\varphi_{DAS})\cos(\varphi_{ray}) + \sin(\varphi_{DAS})\sin(\varphi_{ray})\right) + \sin(\theta_{DAS})^2\sin(2\theta_{DAS})\Big)\psi(x,y,z,t) \\
=& \boxed{\begin{aligned}&\frac{k^2 cA}{2}\Big(-\cos(\theta_{DAS})^2\sin(2\theta_{ray})\cos(\varphi_{DAS}-\varphi_{ray})^2 + \sin(2\theta_{DAS})\cos(2\theta_{ray})\cos(\varphi_{DAS}-\varphi_{ray}) \\ &+ \sin(\theta_{DAS})^2\sin(2\theta_{ray})\Big)\psi(x,y,z,t)\end{aligned}} \\
=& \boxed{\begin{aligned}&k^2 cA\Big(\cos(\theta_{DAS})\cos(\theta_{ray})\cos((\varphi_{DAS}-\varphi_{ray})) + \sin(\theta_{DAS})\sin(\theta_{ray})\Big) \\ &\times\Big(-\cos(\theta_{DAS})\sin(\theta_{ray})\cos((\varphi_{DAS}-\varphi_{ray})) + \sin(\theta_{DAS})\cos(\theta_{ray})\Big)\psi(x,y,z,t)\end{aligned}}
\end{aligned}
$$

To consider the gauge length effect, we average the strain over a linear segment of direction. $[\cos(\varphi_{DAS})\cos(\theta_{DAS}), \sin(\varphi_{DAS})\cos(\theta_{DAS}), \sin(\theta_{DAS})]$ using some steps from 2:

$$
\begin{aligned}
\dot{\epsilon}_{xx'g} =& \frac{1}{g}\int_{\frac{+g}{2}}^{\frac{-g}{2}} \dot{\epsilon}_{xx'}(x + v\cos(\varphi_{DAS})\cos(\theta_{DAS}), y + v\sin(\varphi_{DAS})\cos(\theta_{DAS}), z + v\sin(\theta_{DAS}), t)dv \\
=& \frac{k^2 cA}{g}(\cos(\theta_{DAS})\cos(\theta_{ray})\cos(\varphi_{DAS}-\varphi_{ray}) + \sin(\theta_{DAS})\sin(\theta_{ray})) \\
&(-\cos(\theta_{DAS})\sin(\theta_{ray})\cos(\varphi_{DAS}-\varphi_{ray}) + \sin(\theta_{DAS})\cos(\theta_{ray})) \\
&\int_{\frac{+g}{2}}^{\frac{-g}{2}} e^{ik(ct-(x+v\cos(\varphi_{DAS})\cos(\theta_{DAS}))\cos(\varphi_{ray})\cos(\theta_{ray})-(y+v\sin(\varphi_{DAS})\cos(\theta_{DAS}))\sin(\varphi_{ray})\cos(\theta_{ray})-(z+v\sin(\theta_{DAS}))\sin(\theta_{ray})}dv \\
=& \frac{2k^2 cA}{kg}\frac{(\cos(\theta_{DAS})\cos(\theta_{ray})\cos(\varphi_{DAS}-\varphi_{ray}) + \sin(\theta_{DAS})\sin(\theta_{ray}))(-\cos(\theta_{DAS})\sin(\theta_{ray})\cos(\varphi_{DAS}-\varphi_{ray})}{(\cos(\theta_{ray})\cos(\theta_{DAS})\cos(\varphi_{ray}-\varphi_{DAS}) + \sin(\theta_{DAS})\sin(\theta_{ray}))} \\
&+ \frac{\sin(\theta_{DAS})\cos(\theta_{ray}))}{(\cos(\theta_{ray})\cos(\theta_{DAS})\cos(\varphi_{ray}-\varphi_{DAS}) + \sin(\theta_{DAS})\sin(\theta_{ray}))} \\
&sin(\frac{kg}{2}(\cos(\theta_{DAS})\cos(\theta_{ray})\cos(\varphi_{DAS}-\varphi_{ray}) + \sin(\theta_{DAS})\sin(\theta_{ray})))\psi(x,y,z,t) \\
=& \boxed{\begin{aligned}&\frac{2ckA}{g}(-\cos(\theta_{DAS})\sin(\theta_{ray})\cos(\varphi_{DAS}-\varphi_{ray}) + \sin(\theta_{DAS})\cos(\theta_{ray})) \\ &\times sin(\frac{kg}{2}(\cos(\theta_{DAS})\cos(\theta_{ray})\cos(\varphi_{DAS}-\varphi_{ray}) + \sin(\theta_{DAS})\sin(\theta_{ray})))\psi(x,y,z,t)\end{aligned}}
\end{aligned}
$$

2 Looped Gauge length sensitivity equations demonstration

2.1 Horizontal loop

For a looped gauge length in the horizontal, the dip ange θ_{DAS} is zero. To compute the averaged strain rate for each wave polarization over the loop, we evaluate:

$$\frac{1}{g}\oint \dot{\epsilon}_{xx'}\, d\varphi_{DAS}$$

Since the gauge length is a circular loop, its length can be rewritten as $g = 2\pi R$, where R is the loop radius. We assume here that the wavelength is much larger than the loop size

2.1.1 P Waves

From the point strain-rate sensitivity of a linear DAS segment, the strain rate due to P-waves is given by:

$$\dot{\epsilon}_{Pxx'} = k^2 cA(\cos(\theta_{DAS})\cos(\theta_{ray})\cos(\varphi_{DAS}-\varphi_{ray}) + \sin(\theta_{DAS})\sin(\theta_{ray}))^2\psi(x,y,z,t)$$

Since $\theta_{DAS} = 0$:

$$\dot{\epsilon}_{Pxx'} = k^2 cA(\cos(\theta_{ray})\cos(\varphi_{DAS}-\varphi_{ray}))^2\psi(x,y,z,t)$$

Averaging over the loop:

$$\begin{aligned}\dot{\epsilon}_{H-P} &= \frac{k^2 cA}{2\pi R}\cos(\theta_{ray})^2\,\psi(x,y,z,t)\oint \cos(\varphi_{DAS}-\varphi_{ray})^2\, d\varphi_{DAS}\\ &= \frac{k^2 cA}{2\pi R}\cos(\theta_{ray})^2\,\psi(x,y,z,t)\oint (\frac{1}{2}+\frac{1}{2}\cos(2(\varphi_{DAS}-\varphi_{ray})))d\varphi_{DAS}\end{aligned}$$

Evaluating the integral over one full loop (0 to 2π):

$$\oint \cos(2(\varphi_{DAS}-\varphi_{ray}))\, d\varphi_{DAS} = 0 \quad \text{and} \quad \oint 1\, d\varphi_{DAS} = 2\pi$$

Therefore:

$$\begin{aligned}\dot{\epsilon}_{H-P} &= \frac{k^2 cA}{2\pi R}\cos(\theta ray)^2\,\frac{1}{2}2\pi\psi(x,y,z,t)\\ &= \boxed{\frac{k^2 cA}{2R}\cos(\theta ray)^2\,\psi(x,y,z,t)}\end{aligned}$$

2.1.2 SH Waves

From the point strain-rate sensitivity of a linear DAS segment, the strain rate due to SH-waves is given by:

$$\begin{aligned}\dot{\epsilon}_{SHxx'} =& k^2 cA(\cos(\theta_{DAS})\sin(\varphi_{ray}-\varphi_{DAS}))(\cos(\theta_{DAS})\cos(\theta_{ray})\cos(\varphi_{DAS}-\varphi_{ray}))\\ &+(\sin(\theta_{DAS})\sin(\theta_{ray}))\psi(x,y,z,t)\end{aligned}$$

Since $\theta_{DAS} = 0$, this simplifies to:

$$\begin{aligned}\dot{\epsilon}_{SHxx'} &= k^2 cA\sin(\varphi_{ray}-\varphi_{DAS})\cos(\theta_{ray})\cos(\varphi_{DAS}-\varphi_{ray})\,\psi(x,y,z,t)\\ &= \frac{k^2 cA}{4\pi R}\cos(\theta_{ray})\sin(2(\varphi_{ray}-\varphi_{DAS}))\;\psi(x,y,z,t)\end{aligned}$$

The loop-averaged strain rate is given by:

$$\dot{\epsilon}_{H-SH} = \frac{1}{g}\oint \dot{\epsilon}_{SHxx'}\, d\varphi_{DAS}\,\psi(x,y,z,t) = \frac{k^2 cA}{2\pi R}\cos(\theta_{ray})\oint \frac{1}{2}\sin(2(\varphi_{ray}-\varphi_{DAS}))\, d\varphi_{DAS}\,\psi(x,y,z,t)$$

Since the integral of the sine function over a full circular loop vanishes:

$$\oint \sin\left(2(\varphi_{ray} - \varphi_{DAS})\right) d\varphi_{DAS} = 0$$

Therefore, the loop-averaged SH-wave strain rate is:

$$\boxed{\dot{\epsilon}_{H-SH} = 0}$$

2.1.3 SV Waves

From the point strain-rate sensitivity of a linear DAS segment, the strain rate due to SV-waves is given by:

$$\begin{aligned}\dot{\epsilon}_{SVxx'} =& k^2 cA(-\cos(\theta_{DAS})\sin(\theta_{ray})\cos(\varphi_{DAS} - \varphi_{ray}) + \sin(\theta_{DAS})\cos(\theta_{ray}))(\cos(\theta_{DAS})\cos(\theta_{ray})\cos(\varphi_{DAS} - \varphi_{ray}) \\ &+ \sin(\theta_{DAS})\sin(\theta_{ray}))\psi(x, y, z, t)\end{aligned}$$

Since $\theta_{DAS} = 0$, we have $\cos\theta_{DAS} = 1$ and $\sin\theta_{DAS} = 0$. Substituting:

$$\begin{aligned}\dot{\epsilon}_{SVxx'} &= k^2 cA(-\sin(\theta_{ray})\cos(\varphi_{DAS} - \varphi_{ray}))(\cos(\theta_{ray})\cos(\varphi_{DAS} - \varphi_{ray}))\psi(x, y, z, t) \\ &= -k^2 cA\sin(\theta_{ray})\cos(\theta_{ray})\cos(\varphi_{DAS} - \varphi_{ray})^2\,\psi(x, y, z, t) \\ &= -\frac{k^2 cA}{4\pi R}\sin(2\theta_{ray})\,(\frac{1}{2} + \frac{1}{2}\cos(2(\varphi_{DAS} - \varphi_{ray})))\end{aligned}$$

Using the identity:

$$\cos^2(x) = \frac{1}{2} + \frac{1}{2}\cos(2x), \quad \sin(x)\cos(x) = \frac{1}{2}\sin(2x)$$

we write the loop-averaged strain rate as:

$$\begin{aligned}\dot{\epsilon}_{H-SV} &= \frac{1}{g}\oint \dot{\epsilon}_{SVxx'}\, d\varphi_{DAS} \\ &= -\frac{k^2 cA}{4\pi R}\sin(2\theta_{ray})\oint(\frac{1}{2} + \frac{1}{2}\cos(2(\varphi_{DAS} - \varphi_{ray})))d\varphi_{DAS}\end{aligned}$$

Evaluating the integral:

$$\oint(\frac{1}{2} + \frac{1}{2}\cos(2(\varphi_{DAS} - \varphi_{ray})))d\varphi_{DAS} = \frac{1}{2}\cdot 2\pi + \frac{1}{2}\cdot 0 = \pi$$

Therefore:

$$\begin{aligned}\dot{\epsilon}_{H-SV} &= -\frac{k^2 cA}{2\pi R}\frac{1}{2}\sin(2\theta_{ray})\,\pi\psi(x, y, z, t) \\ &= \boxed{-\frac{k^2 cA\sin(2\theta_{ray})}{4R}\psi(x, y, z, t)}\end{aligned}$$

2.2 Vertical Loop

For a vertical loop contained in a plane with orientation φ_{DAS}, we evaluate the loop-averaged strain rate over all dip θ_{DAS}:

$$\frac{1}{g}\oint \dot{\epsilon}_{xx'}\, d\theta_{DAS}$$

Since the gauge length forms a circular loop, it can be written as $g = 2\pi R$, with R being the loop's radius. We assume a wavelengthis much larger than the loop size

2.2.1 P Waves

From the point strain-rate sensitivity of a linear DAS segment, the strain rate due to P-waves is given by:

$$\dot{\epsilon}_{Pxx'} = k^2 cA(\cos(\theta_{DAS})\cos(\theta_{ray})\cos(\varphi_{DAS}-\varphi_{ray}) + \sin(\theta_{DAS})\sin(\theta_{ray}))^2\,\psi(x,y,z,t)$$

Averaging over the vertical loop yields:

$$\begin{aligned}\dot{\epsilon}_{H-P} =& \frac{k^2cA}{2\pi R}\oint(\cos(\theta_{DAS})\cos(\theta_{ray})\cos(\varphi_{DAS}-\varphi_{ray}) + \sin(\theta_{DAS})\sin(\theta_{ray}))^2 d\theta_{DAS}\,\psi(x,y,z,t)\\ =& \frac{k^2cA}{2\pi R}\oint(\cos(\theta_{DAS})^2\cos(\theta_{ray})^2\cos(\varphi_{DAS}-\varphi_{ray})^2 + 2\cos(\theta_{DAS})\cos(\theta_{ray})\cos(\varphi_{DAS}-\varphi_{ray})\sin(\theta_{DAS})\sin(\theta_{ray})\\ &+ \sin(\theta_{DAS})^2\sin(\theta_{ray})^2)d\theta_{DAS}\,\psi(x,y,z,t)\end{aligned}$$

We evaluate the three parts of the integral separately:

- First term:

$$\oint \cos(\theta_{DAS})^2\; d\theta_{DAS} = \pi \quad \Rightarrow \quad \pi\cos(\theta_{ray})^2\cos(\varphi_{DAS}-\varphi_{ray})^2$$

- Second term:

$$\oint \cos(\theta_{DAS})\sin(\theta_{DAS})\; d\theta_{DAS} = 0 \quad \Rightarrow \quad \text{this term vanishes}$$

- Third term:

$$\oint \sin(\theta_{DAS})^2\; d\theta_{DAS} = \pi \quad \Rightarrow \quad \pi\sin(\theta_{ray})^2$$

Substituting:

$$\begin{aligned}\dot{\epsilon}_{H-P} &= \frac{k^2cA}{2\pi R}(\pi\cos(\theta_{ray})^2\cos(\varphi_{DAS}-\varphi_{ray})^2 + \pi\sin(\theta_{ray})^2)\,\psi(x,y,z,t)\\ &= \boxed{\frac{k^2cA}{2R}(\cos(\theta_{ray})^2\cos(\varphi_{DAS}-\varphi_{ray})^2 + S^2_{\theta_{ray}})\,\psi(x,y,z,t)}\end{aligned}$$

2.2.2 SH waves

From the point strain-rate sensitivity of a linear DAS segment, the strain rate due to SH-waves is given by:

$$\dot{\epsilon}_{SHxx'} = k^2cA(\cos(\theta_{DAS})\sin(\varphi_{ray}-\varphi_{DAS}))(\cos(\theta_{DAS})\cos(\theta_{ray})\cos(\varphi_{DAS}-\varphi_{ray}) + \sin(\theta_{DAS})\sin(\theta_{ray}))\psi(x,y,z,t)$$

Averaging over the vertical loop yields:

$$\begin{aligned}\dot{\epsilon}_{SHxx'} &= \frac{k^2cA}{g}\oint(\cos(\theta_{DAS})\sin(\varphi_{ray}-\varphi_{DAS}))(\cos(\theta_{DAS})\cos(\theta_{ray})\cos(\varphi_{DAS}-\varphi_{ray}) + \sin(\theta_{DAS})\sin(\theta_{ray}))\,d\theta_{DAS}\,\psi(x\\ &= \frac{k^2cA}{g}\oint\cos(\theta_{DAS})^2\cos(\theta_{ray})\;\frac{\sin(2(\varphi_{DAS}-\varphi_{ray}))}{2} + \frac{\sin(2\theta_{DAS})}{2}\sin(\theta_{ray})\;d\theta_{DAS}\,\psi(x,y,z,t)\end{aligned}$$

We evaluate the three parts of the integral separately:

- First term:

$$\oint \cos(\theta_{DAS})^2\;\cos(\theta_{ray})\;\frac{\sin(2(\varphi_{DAS}-\varphi_{ray}))}{2}\,d\theta_{DAS} = \pi\;\cos(\theta_{ray})\;\frac{\sin(2(\varphi_{DAS}-\varphi_{ray}))}{2}$$

- Second term:

$$\oint \frac{\sin(2\theta_{DAS})}{2} \sin(\theta_{ray})\ d\theta_{DAS} = 0$$

Substituting into the averaged expression:

$$\begin{aligned}\dot{\epsilon}_{SHxx'} &= \frac{k^2 cA}{2\pi R}\pi\ \cos(\theta_{ray})\ \frac{\sin(2(\varphi_{DAS}-\varphi_{ray}))}{2}\,\psi(x,y,z,t)\\ &= \boxed{\frac{k^2 cA}{4R}\ \cos(\theta_{ray})\ \sin(2(\varphi_{DAS}-\varphi_{ray}))\ \psi(x,y,z,t)}\end{aligned}$$

2.2.3 SV waves

From the point strain-rate sensitivity of a linear DAS segment, the strain rate due to SV-waves is given by:

$$\begin{aligned}\dot{\epsilon}_{SVxx'} =& k^2 cA(-\cos(\theta_{DAS})\sin(\theta_{ray})\cos(\varphi_{DAS}-\varphi_{ray}) + \sin(\theta_{DAS})\cos(\theta_{ray}))(\cos(\theta_{DAS})\cos(\theta_{ray})\cos(\varphi_{DAS}-\varphi_{ray})\\ &+ \sin(\theta_{DAS})\sin(\theta_{ray}))\,\psi(x,y,z,t)\end{aligned}$$

Averaging over the vertical loop:

$$\begin{aligned}\dot{\epsilon}_{SVxx'} =& \frac{k^2 cA}{g}\oint(-\cos(\theta_{DAS})\sin(\theta_{ray})\cos(\varphi_{DAS}-\varphi_{ray})\\ &+ \sin(\theta_{DAS})\cos(\theta_{ray}))(\cos(\theta_{DAS})\cos(\theta_{ray})\cos(\varphi_{DAS}-\varphi_{ray}) + \sin(\theta_{DAS})\sin(\theta_{ray}))\,d\theta_{DAS}\,\psi(x,y,z,t)\end{aligned}$$

Expanding the product within the integral gives:

$$\begin{aligned}\dot{\epsilon}_{SVxx'} = \frac{k^2 cA}{g}\oint &-\cos(\theta_{DAS})\,\frac{\sin(2\theta_{ray})}{2}\cos(\varphi_{DAS}-\varphi_{ray})^2 - \frac{\sin(2\theta_{DAS})}{2}\ \sin(\theta_{ray})^2\ \cos(\varphi_{DAS}-\varphi_{ray})\\ &+ \frac{\sin(2\theta_{DAS})}{2}\ \cos(\theta_{ray})^2\ \cos(\varphi_{DAS}-\varphi_{ray}) + \sin(\theta_{DAS})^2\,\frac{\sin(2\theta_{ray})}{2}\,d\theta_{DAS}\,\psi(x,y,z,t)\end{aligned}$$

We evaluate the three parts of the integral separately:

- First term:

$$\oint -\cos(\theta_{DAS})\,\frac{\sin(2\theta_{ray})}{2}\cos(\varphi_{DAS}-\varphi ray)^2\ d\theta_{DAS} = -\pi\frac{\sin(2\theta_{ray})}{2}\cos(\varphi_{DAS}-\varphi ray)^2$$

- Second term:

$$\oint -\frac{\sin(2\theta_{DAS})}{2}\ \sin(\theta_{ray})^2\ \cos(\varphi_{DAS}-\varphi_{ray})\ d\theta_{DAS} = 0$$

- Third term:

$$\oint \frac{\sin(2\theta_{DAS})}{2}\ \cos(\theta_{ray})^2\ \cos(\varphi_{DAS}-\varphi_{ray})\ d\theta_{DAS} = 0$$

- Fourth term:

$$\oint \sin(\theta_{DAS})^2\,\frac{\sin(2\theta_{ray})}{2}\,d\theta_{DAS} = \pi\frac{\sin(\theta_{ray})}{2}$$

Substituting:

$$\begin{aligned}\dot{\epsilon}_{SVxx'} &= \frac{k^2 cA}{2\pi R}\left(\frac{-\pi\ \sin(\theta_{ray})\ \cos(\varphi_{DAS}-\varphi_{ray})^2}{2} + \frac{\pi\ \sin(\theta_{ray})}{2}\right)\psi(x,y,z,t)\\ &= \boxed{\frac{k^2 cA}{4R}\sin(\theta_{ray})\sin(\varphi_{DAS}-\varphi_{ray})^2\ \psi(x,y,z,t)}\end{aligned}$$

3 Ray tracing

To evaluate the accuracy and determine the optimal parameters for the ray tracing step using `Pykonal`, we adopt a synthetic-based approach. This allows us to systematically test how grid parameters influence ray stability as well as the intrinsic error of the method.

3.1 Experimental Setup

For this sensitivity analysis, we consider 10,000 randomly distributed source–receiver pairs within a 1 km^3 velocity model. The model follows a checkerboard design, where the velocity varies in cubic blocks. It is constructed by adding cubes whose dimensions and velocity values are listed in table 1 and indicated by the vertical lines in figure 1 subplots A and C.

To ensure the high-frequency assumption required for the derivation of the Eikonal equations, we apply a low-pass filter characterized by an attenuation of 0.99 at 30 m. This is implemented as a convolution with a Gaussian window whose standard deviation is given by equation 3. The corresponding attenuation response is shown in figure 1 subplot C.

$$\epsilon = \frac{D}{\pi}\sqrt{-2\ln(0.99)}\,. \tag{3}$$

Cube size (m)	5	15	20	25	30	35	40	45	100
Velocity (m/s)	100	100	100	100	100	100	100	100	1000
Velocity delta (Δv)	100	100	100	100	100	100	100	100	100

Table 1: Parameters of the checkerboard velocity model.

For each source–receiver pair, we monitor ray divergence while varying only the spatial sampling of the velocity grid. Since `Pykonal` uses a quarter of the grid spacing as the step size to compute the travel-time gradient and ray path, modifying the grid resolution directly affects the ray sampling.

Ray divergence is defined both at the source and at the receiver as the angle between the reference ray, computed at the finest sampling, and the current ray. In addition, we evaluate global divergence by computing the Euclidean distance between corresponding nodes along the ray paths.

3.2 Results

From the median divergence across all source–receiver pairs for each grid sampling reveals that rays remain stable for step sizes up to half the filter length (figure 1 subplot A), corresponding to a node spacing of about 60 m. To estimate the error inherent to the method, we restricted the analysis to rays that converged (step size < 15 m). For each source-receiver pair, we estimate the error through the standard deviation of the angles between the rays at the source and receiver across all different grid sampling and compiled the distribution of these values over the 10,000 realizations. At the source, the mode of the standard deviation is $0.59°$(figure1 subplot D), while at the receiver it is $3.30°$ figure 1 subplot E. The receiver-side distribution also exhibits a long tail with larger standard deviations, which we attribute to cases where multiple ray paths are possible and travel-time discretizations affects path selection. Moreover, both the source incidence angle and the Euclidean travel distance increase monotonically with step size, likely due to the straightening of ray paths steps are getting larger.

Because computational cost scales as a cube in regard to step size (figure1 subplot B), selecting an optimal grid resolution is crucial. Particularly since the ray path must be computed for each DAS channel independently.

These results represent a first-order approximation: the model heterogeneity all share the same amplitude, and errors are not expressed as a function of ray length, both of which may influence the conclusions.

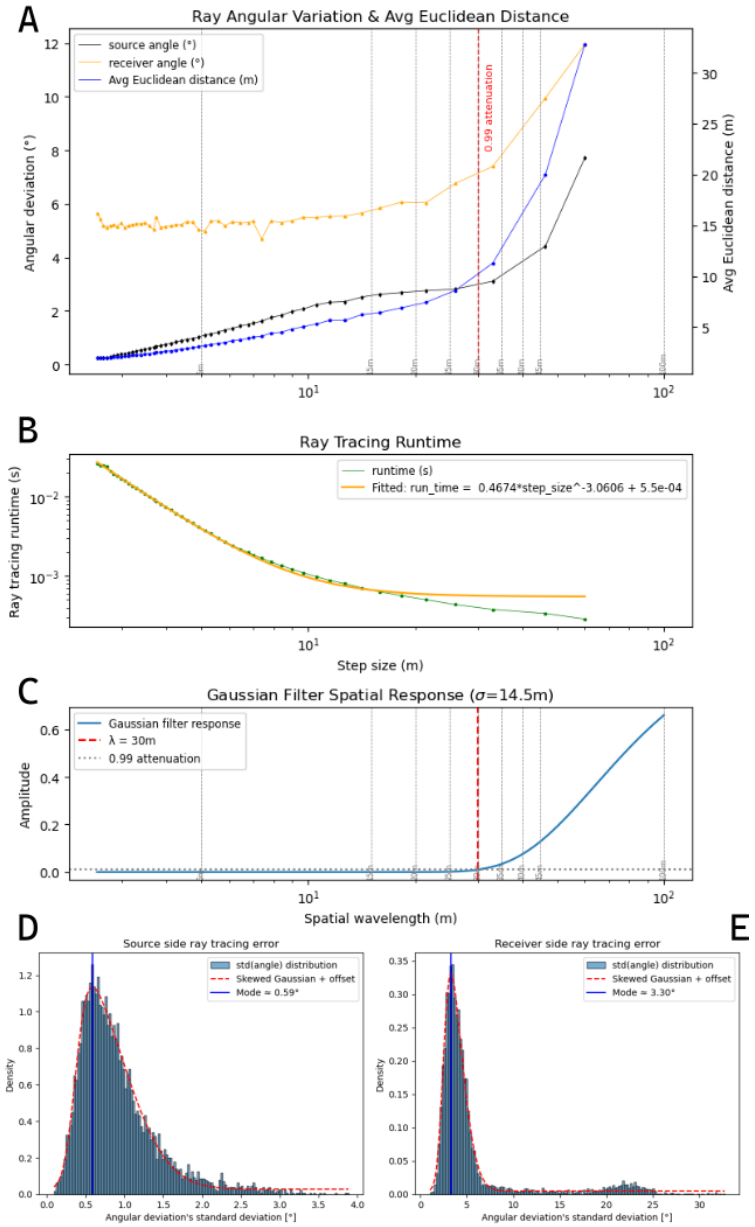

Figure 1: A: Average angular deviation at the source (black) and receiver (orange) in degrees, along with the average Euclidean distance between nodes along the rays in meters. Theses deviation are measured between the any ray and the most resolved one. The model space is based of a source-receiver ensemble consisting of 10,000 randomly distributed pairs, placed within a 1 km^3 velocity model exhibiting a checkerboard pattern summarized in table 1. B: Average run time per ray tracing operation for a given step size with the best fitting polynomial function. C : Low-pass filter spatial response. The filter is characterized by an attenuation factor of 0.99 at 30 m. Vertical lines in the panel A and B indicate the scale of heterogeneities (as in table 1) in the model. D - E : Histograms of the angular errors due to the grid spatial sampling over the 10.000 realzsation. This error is estimated from each realization using standard deviation of the between the rays at the source and receiver over all the step sizes smaller than 15 m. The distribution mode is 0.59° at the source and 3.3° at the receiver. The non-zero baseline in the receiver histogram reflects the influence of multi path effects.